RICE UNIVERSITY

Ultrafast and Magneto-Optical Spectroscopy of Semiconductor Heterostructures

by

Gary Timothy Noe II

A Thesis Submitted
in Partial Fulfillment of the
Requirements for the Degree

Master of Science

Approved, Thesis Committee:

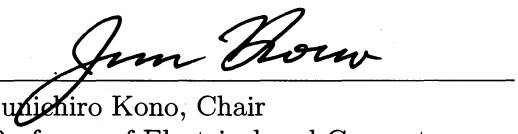

Junichiro Kono, Chair
Professor of Electrical and Computer
Engineering and Physics and Astronomy

Daniel M. Mittleman
Professor of Electrical and Computer
Engineering

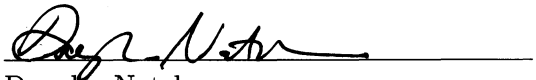

Douglas Natelson
Professor of Physics and Astronomy

Houston, Texas

June, 2011

ABSTRACT

Ultrafast and Magneto-Optical Spectroscopy of Semiconductor Heterostructures

by

Gary Timothy Noe II

This thesis presents spectroscopic results using semiconductor heterostructures important for both applied and fundamental physics. First, we studied short-period superlattices of InAs and GaSb that suggest a promising alternative to mercury cadmium telluride for mid-infrared detection. Our time-domain measurements help sample growers optimize growth conditions to maximize the carrier lifetime and determine the superlattice period and interface quality. The second area of research has a more fundamental focus. Here, we study the time-integrated emission and time-resolved population and emission properties of high-density excitons in an InGaAs quantum well sample in strong perpendicular magnetic field. Our time-integrated results indicate that two-dimensional magneto-excitons can appear to be stable against a Mott transition with the application of magnetic field. Our time-resolved results provide the first direct observation of superfluorescence using a semiconductor showing the population inversion of magneto-excitons suddenly drop from fully excited to completely unexcited emitting an intense pulse of coherent radiation.

Acknowledgments

First off, I would like to thank my advisor, Professor Junichiro Kono, for his guidance and support throughout the course of my time under his mentorship. He has provided fantastic opportunities for me to engage in exciting research which I will forever reflect upon with great nostalgia. Thank you to the other members of my thesis committee, Dr. Daniel Mittleman and Dr. Douglas Natelson, for agreeing to serve on my committee.

I would also like to thank my wife, Gigi, for putting up with me when I stayed in the lab well into the night, traveled to the magnet lab for weeks away from home, and stressed over deadlines and work-related obligations. She is a perfect companion for a guy like me. Thanks go to my two daughters, Vivian and baby Emma, for filling my life with joy and a welcome distraction from research. I would like to thank my father, mother, sisters, Stephanie and Beth, and brother, Bryce, for their continuing support and confidence in me.

Finally, I would like to thank my fellow colleagues for their willingness to give advice or provide physical labor whenever I asked. Especially, I would like to thank Steve McGill and Jinho Lee for their great contributions with the time-resolved measurements using the superconducting magnet in Tallahassee. I thank our collaborators, Chris Stanton and Alexey Belyanin, for providing a solid theoretical framework for understanding our experimental results. I would like to thank our collaborators, Heather Haugan and Gail Brown. Thank you to Judy Cherian, Takahisa Tokumoto, and Dmitry Semenov for their help setting up the experiment. I thank my fellow Kono group members: Chanjuan Sun, Bill Rice, Darius Morris, Thomas Searles, Layla Booshehri, Erik Haroz, Ajit Srivastava, Takashi Arikawa, Sebastien Nanot, Ji-

hee Kim, Xuan Wang, Lei Ren, Qi Zhang, Xiangfeng Wang, and Jonah Shaver. It has been a great pleasure to work alongside all of you.

Contents

Illustrations

Tables

Chapter 1

Introduction

The use of spectroscopy to study semiconductor heterostructures is important for both applied and fundamental physics. Short-period superlattice (SL) samples based on alternating layers of InAs and GaSb are a promising candidate for replacing mercury cadmium telluride (MCT) as the material system of choice for mid-infrared (IR) detection. The band gap of this Type II "broken gap" multiple-quantum-well structure can be tuned to a specified mid-IR wavelength by the appropriate choice of SL period. The major advantage of this material over MCT is the possibility of functioning at high operating temperatures instead of cryogenic temperatures that is required for MCT detectors and other devices for mid-IR detection. Although this material shows promise, the fabrication of high-quality detectors using these SLs remains challenging, and many material properties are not well understood. We have been working with sample growers to help identify how the growth parameters affect certain material properties. In Chapter 2 of this thesis, we present progress on our measurements of the overall carrier lifetime and coherent phonon dynamics towards the goal of providing useful information to help determine the appropriate growth parameters to create a functional mid-IR detector using these SL structures at high operating temperatures.

The two-dimensional electron-hole system in semiconductor quantum well samples becomes fully quantized when placed in a perpendicular magnetic field. This experimental setting provides an extremely rich system to explore unique phenom-

ena. In Chapter 3, we present time-integrated absorption and emission results that show that two-dimensional magneto-excitons are stable against a Mott transition with the application of a finite magnetic field. In high magnetic fields, a theoretically predicted "hidden symmetry" for two-dimensional magneto-excitons is expected, where all inter-exciton interactions exactly cancel, preventing a Mott transition to an electron-hole magnetoplasma. Our results extend this prediction as our results show excitonic character at all magnetic fields besides zero. In Chapter 4, we present time-resolved absorption and emission results that show strong evidence for superfluorescence (SF) under the conditions of high density of excitons, high magnetic field, and low temperature. These results mark the first direct observation of SF in a semiconductor quantum well system. Before going into the details of the above mentioned experiments and results, a general introduction to the relevant topics will first be presented.

1.1 Semiconductor Heterostructures and Alloys

Semiconductors are materials with band gap separating a full valence band and empty conduction band. Their transport properties are somewhere between an insulator and conductor. This allows them to be very useful in terms of controlling their electronic properties and, hence, their importance in device applications. Since the invention and subsequent development of the transistor in the 1950s, semiconductor devices have revolutionized the way in which we live, creating ever so smaller and portable devices that have made their way into our everyday lives. From communications to computation and beyond, almost every device considered high technology has some kind of semiconductor device that is essential to its functionality. Laser diodes were originally developed in the early 1960s using GaAs junctions [10, 11]. It was not until

after Herbert Kroemer proposed the use of a heterojunction injection laser that semiconductor heterostructures became the preferred method of creating a laser diode [12]. Later, the development of molecular beam epitaxy (MBE) allowed for the growth of compound semiconductor films with much improved control and the possibility to create abrupt changes in material species for creating heterostructures with high quality interfaces [13]. MBE and other precision growth techniques allow the engineer to modify the band structure of semiconductor materials in order to tune the electronic and optical properties to create the ideal material system for a given application. The most important inventions based on semiconductor heterostructures are semiconductor lasers and photodetectors which are essential for optical communications.

A rich variety of semiconductor heterostructures and alloys can be created via the process of MBE. A semiconductor alloy consists of two or more semiconductors that are mixed together to create a new composite material. Most commonly these materials are mixed together randomly so that one of the types of atoms has a given probability of being next to the other type of atom. Alloying is useful because it allows one to alter the band gap of the material. Figure 1.1 shows the band gap vs. lattice constant for various group IV fundamental and III-V compound semiconductor materials. Creating an alloy of two semiconductor materials will result in a mix of properties for both semiconductors. The lines between two semiconductor materials in Figure 1.1 show the available band gap and lattice constant when creating an alloy. For instance, the alloy $In_{0.2}Ga_{0.8}As$ will have an energy gap and lattice constant between the respective values for GaAs and InAs.

Semiconductor heterostructures are formed when two different semiconductors are grown next to each other with an abrupt interface between them. Forming semiconductor heterostructures allows one to modify the electronic properties of semicon-

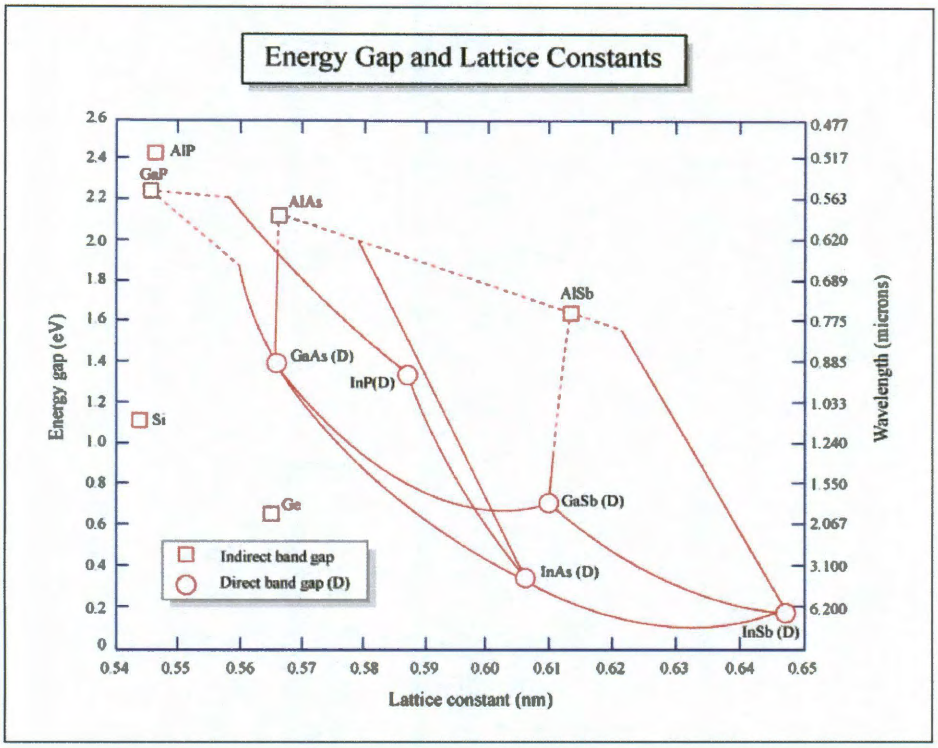

Figure 1.1 : Energy Gap vs Lattice Constant for various group IV fundamental and III-V compound semiconductor materials. Provided by MIT OpenCourseWare.

ductors via quantum confinement effects [14]. In order to reduce strain, growers can create a heterostructure with two or more semiconductor materials that have similar lattice constants. Alternatively, a heterostructure using $In_{0.2}Ga_{0.8}As$ and GaAs will have strain between the layers, which will have some effects on the electronic properties of the heterostructure. Here, I studied two different types of semiconductor heterostructures, a Type I heterostructure and a Type II heterostructure. In Type I heterostructures, the conduction band bottom of semiconductor A is below the conduction band bottom of semiconductor B and the valence band top of semiconductor A is above the valence band top of semiconductor B such that the band gap of the well fits within the large gap of the barrier. In Type II heterostructures, the band

gap of one of the materials does not fit within the band gap of the other material. See

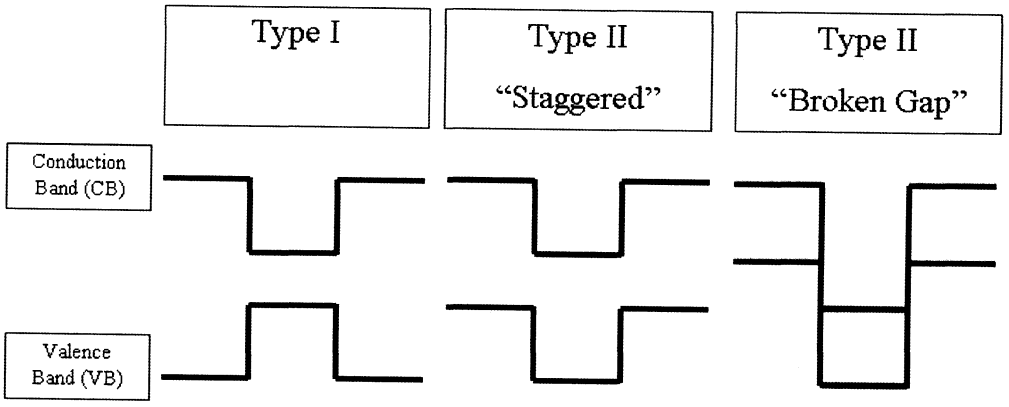

Figure 1.2 : Diagram showing different types of semiconductor heterostructure.

Figure 1.2 for an illustration of these different types of semiconductor heterostructure [15]. The important consequence of the Type II band lineup is that electrons and holes are confined in different layers. A multiple quantum well structure is a periodic structure consisting of layers of two or more semiconductor materials. A superlattice (SL) is a special type of multiple quantum well structure that has some wavefunction overlap between adjacent wells. By creating a sufficiently thin semiconductor quantum well structure, the available energy levels for carriers in the well become quantized as a result of confinement effects similar to the general problem in quantum mechanics of a particle in a box. Semiconductor heterostructures are designed to take advantage of these modifications to the electronic states. By making semiconductor heterostructures and alloying, one can engineer a material with tailored electronic and optical properties.

1.2 Ultrafast Spectroscopy

The use of ultrafast spectroscopy provides a means to study processes or events that occur on timescales much smaller than the timescales accessible to electronics. The highest speed electronics offer frequency response in the GHz range which means that the fastest response times are on the order of 100s of picoseconds to 1 nanosecond. The shortest ultrafast pulses ever generated to date are on the order of 100 attoseconds, centered in the x-ray frequency range or extreme ultraviolet. This is six orders of magnitude faster than the fastest electronics. Furthermore, the use of ultrafast techniques such as THz time-domain spectroscopy allows researchers to generate and measure the THz response of various materials, opening up the range that was once considered the "technological gap" between optics and electronics [16]. Finally, ultrafast spectroscopy allows one to observe carrier and lattice dynamics in real time to directly determine lifetimes and scattering times in order to elucidate various interactions among microscopic objects in matter. Typical scattering times in solids are measured in picoseconds or shorter, thus requiring ultrafast spectroscopy techniques.

For any experiment with ultrafast lasers, the minimum time resolution is ultimately determined by the width of the laser pulse. The development of ultrafast lasers over the last 50 or 60 years has seen progress from nanosecond to femtosecond and, now, attosecond pulses. These lasers provide researchers with the ability to study dynamics in a wide variety of systems from the relatively slow relaxations in atomic systems to very fast chemical reactions. Furthermore, the peak power during the laser pulse can be extremely high, which opens up the possibility to study and utilize the nonlinear optical properties of various materials. In semiconductor materials, by exciting a very large number of carriers in a very short amount of time, one can study the affects of a high density of carriers without damaging the sample when

the equivalent high peak power of longer laser pulses would damage the sample.

For the work contributing to this thesis, we utilized two different types of laser systems. For measuring small changes in reflectivity, we used a Ti:sapphire oscillator system with ~100 MHz repetition rate, ~80 fs pulse width, and ~1 nJ pulse energy. For measuring long range dynamics and non-linear dynamics, we used amplified Ti:sapphire laser systems with ~1 kHz repetition rate, ~150 fs pulse width, and ~1 mJ pulse energy. Also, with the amplified Ti:sapphire laser systems, we used an optical parametric amplifier (OPA), which utilizes nonlinear optical processes to provide tunable pulsed radiation in the near- and mid-IR. We used two different types of ultrafast techniques to study time dynamics. We used the traditional delay stage pump-probe method where the pump excites or modifies the electronic distribution of carriers in a semiconductor sample and the reflectivity or transmissivity of a weak probe changes in response to the pump. We also used a streak camera with 2 ps resolution to measure time-resolved photoluminescence after ultrafast excitation.

With these techniques and ultrafast laser sources, we were able to measure the full non-equilibrium carrier and phonon dynamics of short-period SLs samples. Our time-integrated measurements on InGaAs quantum wells utilized the high peak power available in ultrafast sources to simultaneously generate large populations of magneto-excitons in order to study their nonlinear emission properties. Furthermore, using time-resolved methods, we were able to measure the population and emission dynamics of magneto-excitons as a function of magnetic field, temperature, and laser intensity to show strong evidence for SF.

1.3 Non-Equilibrium Carrier Dynamics in Semiconductors

After a semiconductor material is excited by an ultrafast laser pulse, the photo-excited carriers undergo a series of relaxation processes. These processes can be broadly outlined even though they overlap temporally. First, there is a coherent regime where the excitations in the semiconductor have a well-defined phase relationship with the exciting laser pulse. Various scattering processes such as carrier-carrier and carrier-phonon scattering in semiconductors typically destroys this coherence rapidly relative to the coherent regime that can be created in atomic and molecular systems. Use of femtosecond techniques is generally required to study this regime in semiconductors. Next, there is a non-thermal regime where the photo-excited carriers have a distribution that cannot be characterized by a temperature using Fermi-Dirac statistics (or Bose-Einstein statistics in the case of excitons). Typical proceses in this regime include electron-hole scattering, carrier capture in quantum wells, and electron-optical phonon scattering. Then, the carriers thermalize to have a distribution that can be characterized by a temperature. This temperature is usually much higher than the lattice temperature, and therefore, this regime is called the hot-carrier regime. Typical processes in this regime include hot-carrier phonon scattering and carrier-acoustic phonon scattering. Finally, there is an isothermal regime where all of the carriers and phonons are in equilibrium with each other and can be characterized by the same temperature of the lattice. Carrier recombination and other slow relaxation mechanisms occur during this regime to bring the photo-excited carriers back to their ground state [17].

For our measurements on short-period Type II SLs, we observe the process of carrier capture in quantum wells, followed by carrier-acoustic phonon scattering resulting in coherent phonon oscillations, and, finally, the slow relaxation process of Auger re-

combination. For our studies of SF, we require the population of magneto-excitons that are initially completely incoherent. This can be ensured as we optically pump high above the barrier, which must be followed by many scattering events before relaxing into the magneto-excitonic levels. Then, the excitons will recombine to emit light with photon energy corresponding to the energy difference between the electron in the conduction band and hole in the valence band.

1.4 High-Density Excitons

An exciton is a bound electon-hole pair. In systems where the effective mass approximation is appropriate, they can be analyzed in a method similar to the hydrogen atom except with a much lower reduced mass. An exciton can be optically created in semiconductors when a photon is absorbed by an electron in the valence band and promoted to the conduction band leaving a hole behind. This electron and hole become bound together via the Coulomb interaction creating an exciton that, after some characteristic lifetime, recombines with the emission of a photon. In the absorption spectrum of the material, there will be a peak in the absorption due to the exciton resonance. With continuous wave (CW) lasers, the rate of generation and rate of recombination of excitons usually balance in a way which leads to a steady-state low-density population of excitons. Using ultrafast lasers, one can simultaneously generate a very large density of excitons, which usually interact with one another before relaxing back to the original ground state. In this high-density regime, there are interesting electronic and emission properties such as band-gap renormalization, ionization of excitons, and superfluorescence. Superfluorescence (SF) is the process of collective coherent emission of radiation by a macroscopic sample of two-level dipoles from an initially incoherent polarization state. SF should be distinguished from super-

radiance (SR), which merely refers to an enhanced recombination rate due to photon exchange between dipoles, without including the spontaneous appearance of macroscopic coherence (one of the most spectacular aspects of SF). The process of SR was originally theoretically proposed by Robert Dicke [18]. In our time-resolved experiments, we study high-density magneto-excitons in a quantum well as the macroscopic sample of two-level dipoles in order to observe SF.

Chapter 2

Carrier and Phonon Dynamics in Short Period InAs/GaSb Superlattices

Currently, the most widely used material systems for mid-IR detection are based on either mercury cadmium telluride (MCT) or quantum well infrared photodetectors (QWIP). Both detectors require cryogenic cooling in order to achieve high sensitivity. With increasing temperature, increased carrier recombination mechanisms in a material tend to reduce the detectivity of a device using them. By increasing the overall carrier lifetime, one should be able to increase the sensitivity of a device. For instance, Auger recombination is known to place an upper limit on detectivity in long wavelength photodetectors [19]. Materials and structures that can produce uncooled, or high operating temperature, detectors in the mid-IR would provide significant advantage over their cryogenically cooled counterparts. In applications such as satellite surveillance, cryogens are not continuously available. Also, cryogenic detectors require a dewar which limits the compactness of the device.

Short-period SL samples based on alternating layers of InAs and GaSb are expected to be an promising material system for mid-IR detection. In order to maintain good optical absorption, the period of the SL should be sufficiently thin. Due to the type-II band alignment of these SLs, the band gap can be tuned to a particular IR range by the appropriate choice of SL period. Also, it is expected that the band structure of these SLs can be designed to reduce Auger recombination to make room temperature operation possible [20]. However, growth and fabrication of high-quality

detectors using InAs/GaSb SLs still remain challenging, and basic material properties, especially dynamic properties, are not well understood. Here, we studied the carrier dynamics for a set of five SL samples with standard ultrafast pump-probe techniques for characterization. All of the measures were at room temperature.

2.1 Superlattice Samples

The samples used in this study were a series of InAs/GaSb SL samples with varied SL period. The conduction band of InAs is lower in energy than the valence band of GaSb, making this a type-II 'broken gap' heterostructure. Based on the SL period, each sample has a different band gap in the IR. Figure 2.1 shows an example band diagram for these samples. Photoexcited electrons and holes are confined in different

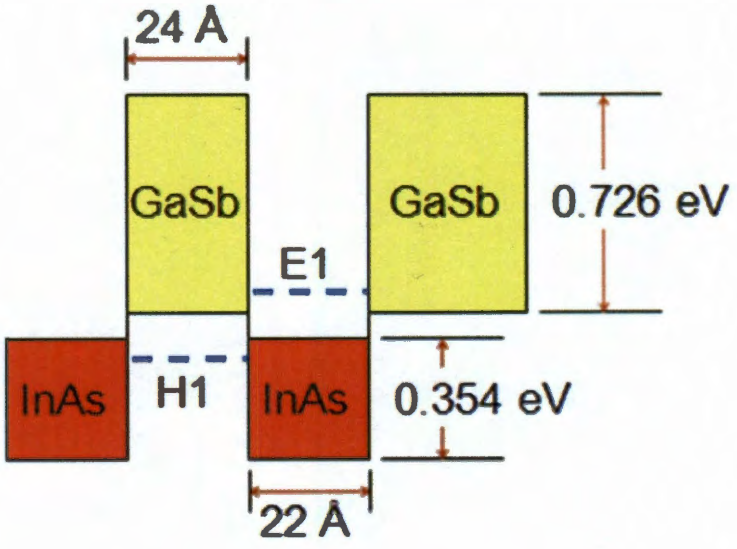

Figure 2.1 : Example band diagram for InAs/GaSb SL structure. Photoexcited electrons and holes are confined in different layers. Because the E_1 and H_1 energy levels depend on the thickness of the layers, the band gap can be tuned by adjusting these layer thickness.

Sample No.	InAs/GaSb (Å/Å) Nominal	SL Period (Å) Nominal	SL Period (Å) X-Ray	Band Gap (eV)
1	21.0/24.0	45	46.0	0.32
2	26.5/21.5	48	49.5	0.22
3	33.5/21.5	55	56.3	0.16
4	38.5/21.5	60	61.0	0.15
5	48.5/21.5	70	71.2	0.09

Table 2.1 : Data summary for the InAs/GaSb SL samples studied in this work. Their nominal thicknesses were estimated from shutter times, and the SL structural parameters where determined by X-ray diffraction. The band gaps are given at a temperature of 10 K.

layers. By adjusting the layer thicknesses, the energy levels, E_1 and H_1, can be tuned to create the desired mid-IR effective band gap. Table 2.1 shows the sample characteristics. For each sample, the number of SL periods was chosen so that the overall thickness of the SL was $\sim$0.5 μm. The SL section was grown on a Te-doped (n-type) GaSb (100) substrate with a 0.3 μm GaSb buffer layer between the SLs and the substrate.

2.2 Long Carrier Lifetime

Because InAs/GaSb superlattices are type-II, photoexcited electrons and holes are confined in different layers. The electron and hole wavefunctions have small overlap. Therefore, the carrier lifetime is expected to be very long, many orders of magnitude longer than MCT samples with the same energy gap [20]. A long carrier lifetime is necessary in order to amplify the photocurrent to increase the sensitivity of a device

using this material. It is expected that this material system maintains good material properties for mid-IR detection at high operating temperatures, maybe even room temperature. Previous studies have measured the time-resolved photoluminescence and the frequency response of the PL to modulation in order to determine the long carrier lifetime [21]. Here, we are using pump-probe techniques to directly measure the carrier lifetimes of these samples.

2.2.1 Measurement Techniques

Traditional Pump-Probe

To measure the carrier dynamics of these samples, we first set up a traditional pump-probe setup using delay stage techniques. The pump in this experiment was an optical parametric amplifier (OPA) that is seeded by an amplified Ti:Sapphire laser. We refer to our amplified Ti:Sapphire laser as a CPA in reference to the process of chirped pulse amplification where a low pulse energy seed pulse becomes amplified to make a short high energy pulse. The output pulse energy of our CPA is 1 mJ at a repetition rate of 1 kHz and 775 nm center wavelength. About 85% of the CPA output is reflected off of a beam splitter to pump the OPA. The OPA is a tunable source of femtosecond radiation with the characteristics outlined in Table 2.2.1.

The remaining 15% of the CPA output is available after the beam splitter. Here, we used the OPA tuned to 1.5 μm as the pump and the CPA as the probe. The basic experimental setup is shown in Figure 2.2. The time delay is introduced by placing corner cubes on a mm motorized 1D stage. For this experiment, we used two long stages, with a length of 300 and 500 mm, respectively, to introduce a long time delay between the pump and probe. The CPA probe passed once with the 300 mm stage and twice with the 500 mm stage for a total available delay of 8.6 ns. The OPA

OPA Source	Tuning Range
Signal	1150-1600 nm
Idler	1600-2600 nm
SH Signal	580-800 nm
SH Idler	800-1150 nm
SF Pump-Idler	533-600 nm
DFG 1	2.4-11 um
DFG 2	5-20 um

Table 2.2 : Typical output characteristic of our TOPAS-800 optical parametric amplifier.

pump was reflected by 90 degrees and focused with a 6 inch parabolic mirror while the CPA probe was incident off axis in order to redirect the reflected light and measure with a fast photodiode. An optical chopper was placed in the path of the OPA to modulate the pump, and the reflected probe was measured with a lock-in amplifier at the modulation frequency. In this way, the pump-induced change in reflected probe light was measured as a function of time delay between pump and probe.

Continuous Wave Probe

Problems such as beam walk and beam divergence make it impractical to introduce an arbitrarily long optical delay. In order to measure carrier dynamics longer than the largest available time delay of 8.6 ns, we needed to come up with a different technique instead of standard delay stage methods. To do this, we used a continuous wave (CW) 658 nm laser diode as the probe instead of the pulsed CPA. The OPA

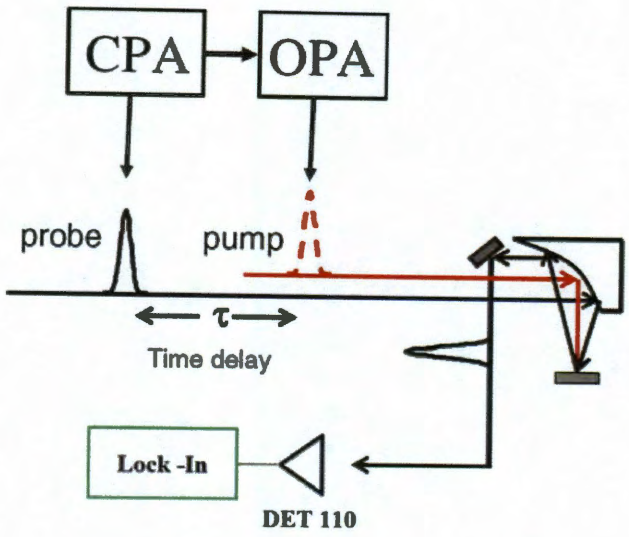

Figure 2.2 : Differential Reflectivity Pump-Probe Setup

was still used as the pump. Before the laser diode beam was incident on the sample, we used a beam splitter to pick off a reference for a balanced detector with 350 MHz bandwidth. The balanced detector measures and amplifies the difference between the reference and the laser diode probe that is reflected off of the sample to remove common mode noise. Using an oscilloscope triggered at the repetition rate of the OPA, we measured this difference directly and averaged over 10,000 waveforms.

2.2.2 Results and Discussion

The initial long scan results, shown in Figure 2.3, indicated that the carrier lifetime was much longer than ~8 ns, our maximum delay between pump and probe. Note that the horizontal axis is split to show the initial dynamics as well as the long carrier decay. Initially, there is a sharp decrease in reflectivity that is due to the carriers becoming trapped in the quantum wells. When the carriers are initially excited,

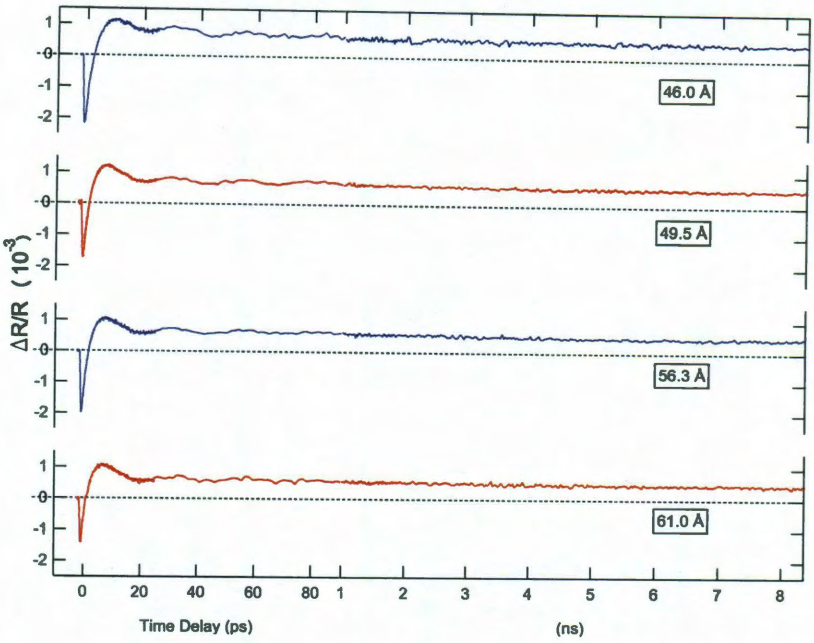

Figure 2.3 : Overall pump-probe differential reflectivity dynamics for 4 samples with varied SL period. The normalized differential reflectivity shows three features: a sharp decrease followed by a sign change taking a few ps, slow oscillations with period of ~24 ps, and a recovery much slower than 8 ns.

because the photon frequency is greater than the plasma frequency, the increase in free carrier density leads to a decrease in the real part of the index that leads to a decrease in reflectivity. Next, there are oscillations with a period of ~24 ps, which we attribute to propagating coherent phonon oscillations. Finally, there is a long recovery much slower than 8 ns. All four samples show very similar results including the period of coherent phonon oscillations. The results from fitting the long decay gave initial estimates of a 30 ns decay constant, but the results of this fit varied wildly with each scan.

In order to successfully get an estimate of the carrier lifetime, we needed to measure the full recovery back to the ground state. Figure 2.4 shows initial results using the CW probe setup. Here we observe two decay components. One decay component

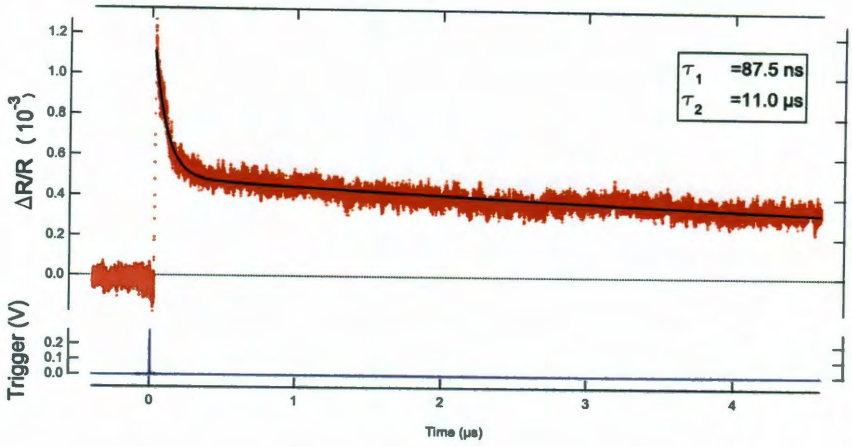

Figure 2.4 : Preliminary long time range differential reflectivity result for the 46 Å sample.

is 87.5 ns, and the other is 11.0 μs. We tentatively interpret the ~90 ns decay as the carrier lifetime because it is on the order of previous results [21]. However, we are not certain about the origin of the very long ~10 μs decay. More work will be needed to determine the origin of all of the decay components.

2.3 Coherent Phonon Dynamics

The ultrafast generation of electrons and holes in the sample by an excitation pulse leads to a strain pulse that perturbs the dielectric function of the sample and propagates at the longitudinal acoustic (LA) sound speed. The sample acts like a Fabry-Perot interferometer, and the period of oscillation is given by

$$T = \frac{\lambda}{2C_s n(\lambda)} \tag{2.1}$$

where λ is the wavelength of the probe, C_s is the LA sound speed, and $n(\lambda)$ is the wavelength-dependent refractive index [22]. For the 46 Å sample, we used the weighted average of the material properties for InAs and GaSb to calculate C_s and

$n(\lambda)$. Using these values, the period of oscillation is 24.8 ps, which is very close to the observed period of 24 ps. Because the samples are all similar in composition, the slow coherent phonon oscillation is similar for all of the samples as seen in Figure 2.3.

In addition to the slow coherent phonon oscillations, it was expected that there exist a fast coherent phonon oscillation with period of $\sim$1 ps, similar to fast oscillations seen previously [23]. The exciting laser pulse generates electron-hole pairs in the quantum wells of the superlattice. This creates a photoexcited carrier distribution that has the periodicity of the superlattice. These carriers can generate coherent acoustic phonon modes with a non-zero frequency and wave vector

$$q = \frac{2\pi}{a} \tag{2.2}$$

where a is the SL period. These fast coherent acoustic phonon oscillations are expected to result in a very small reflection modulation, $\sim 10^{-5}$ or $\sim 10^{-6}$ [24].

2.3.1 Experimental Setup for Coherent Phonon Measurements

Because the fast coherent phonon oscillations result in a very small change in reflectivity, a higher repetition rate laser was used to increase the signal to noise ratio in order to adequately resolve the oscillations. We used a Ti:Sapphire oscillator laser with repetition rate of 93 MHz and pulse width of 80 fs for a degenerate pump-probe setup where the laser beam was split into two arms for the pump and the probe. The pump beam reflected off of a corner cube, which was mounted on a shaker with a delay stage in order to create a fast scanning of the delay time between pump and probe. The probe beam passed a beamsplitter cube so that a reference that does not interact with the sample can be provided to the balanced detector with bandwidth of 125 kHz. The pump and probe beam were focused to the sample such that they

overlaped in space and a time within the range of the shaker. The balanced detector measured the difference in signal between the reference and probe reflected from the sample. By using an A/D converter connected to the output of the shaker for temporal information and the balanced detector for differential reflectivity, we were able to average many scans in a short amount of time. Using this method, we were able to measure changes in reflectivity in the probe to resolve a differential signal of $\sim 10^{-6}$. We used the balanced detector setting, AUTOBALANCE, where the signal generated in both the reference and signal is automatically balanced when they are in close range of each other.

2.3.2 Results and Discussion

After averaging over 5000 scans of the shaker, a clear signal is obtained with great signal to noise ratio. Figure 2.5 shows the differential reflectivity for all five samples. These results are similar to the results shown in Figure 2.3 obtained using the

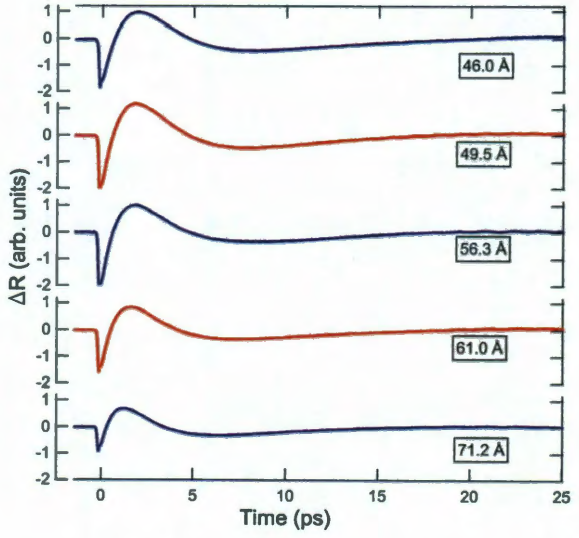

Figure 2.5 : The raw data from the degenerate pump-probe setup with fast scanning shaker for all five samples.

CPA/OPA system in that we see an initial decrease in reflectivity followed by a rise in reflectivity above zero and the beginning of a slow coherent phonon oscillation. The AUTOBALANCE function of the balanced detector responds fast enough to alter these results for the slower features, but the very fast dynamics can still be recovered. Furthermore, the separation between pulses in the pulse train is 10.8 ns, so the differential reflectivity due to the slow carrier dynamics is AUTOBALANCED to zero. After subtracting out the initial electronic component and slow coherent phonon oscillations from the raw data, a very small fast oscillation can be recovered. Figure 2.6 shows the residual differential reflectivity after this fit. From this data, it is clear that

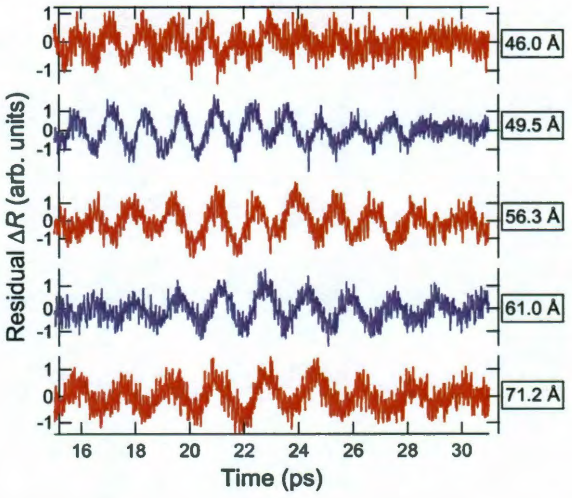

Figure 2.6 : The residual differential reflectivity for different SL-period samples after subtracting the background signal to isolate the fast coherent phonon oscillations. The oscillations show an increase in period with increasing SL period.

the coherent phonon period increases from ~1 ps to ~2 ps with increasing SL period. Figure 2.7 shows the fast Fourier transform (FFT) of these results as a function of SL period. Before taking the FFT, we used a linear interpolation of 10,000 evenly spaced points, zero padding of 90,000 points to increase the data density of the FFT result, and a Hann window function. We see a large peak for each sample, which corresponds

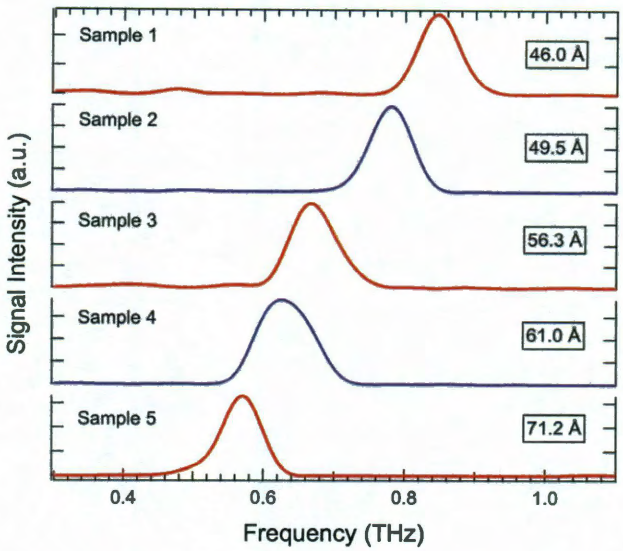

Figure 2.7 : FFT of the fast time-domain oscillations in Figure 2.6. The peak position of the oscillation frequency decreases with increasing SL period.

to the frequency of fast coherent phonons. Because we are using an overall time range of ~16 ps, the resolution of our FFT is limited. If we took data over a longer time range, we should see more features in the FFT, and we would be able to accurately resolve the coherent phonon linewidth [25]. This information can be useful to sample growers as it provides information about the interface quality. After fitting the FFT result with a Gaussian function, the center frequency of the coherent phonons was obtained and plotted against the wave vector, as shown in Figure 2.8. Fitting the angular frequency versus wave vector, q [see Eq. 2.2], provides a value for the acoustic sound velocity of the SL. The value 3.87 x 10^5 cm/s is in between the known values for InAs and GaSb. Alternatively, we can use an average of the two acoustic sound velocities to accurately calculate the SL period.

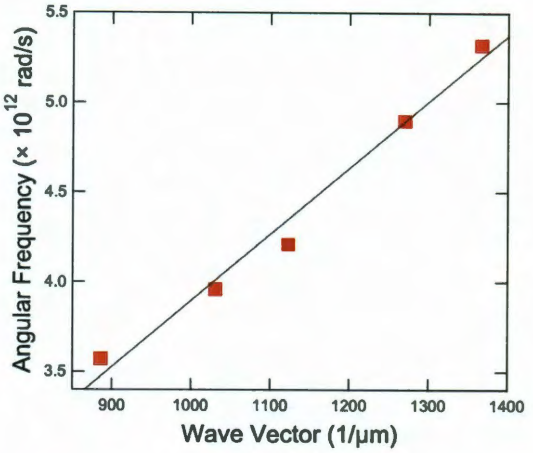

Figure 2.8 : Angular frequency versus wave vector. The slope of the fit corresponds to the sound velocity of 3.87 x 10^5 cm/s

2.4 Conclusion and Future Work

The combined results of these measurements allow us to study the carrier and phonon dynamics spanning roughly 10 orders of magnitude, from the ~80 fs pulse width of the oscillator laser to the 1 ms separation between pulses in the CPA pulse train. We have measured carrier trapping, propagating coherent phonons, fast coherent phonons due to the superlattice, and the long carrier lifetime. Improvements must be made to the CW probe technique in order to provide an accurate comparison of long carrier lifetime for the set of five samples. Additionally, measuring the fast coherent phonon oscillations with a much larger time range should allow us to provide information about the interface quality. This information will help the sample growers adjust their growth parameters to improve the sample for the application of mid-IR detection.

Chapter 3

Photoluminescence and Absorption Properties of High-Density 2D Magneto-Excitons

When matter is placed in a high magnetic field, the electronic states are modified by the quantization of the spin and orbital angular momentum. In semiconductors, high magnetic fields quantize the electronic states of the conduction and valence bands. Here, we study the effect of magnetic fields on 2D excitons in the low- and high-density regimes. Our results show that, with the application of a magnetic field and in the presence of single-pass gain, emission from, what is expected to be, a high-density electron-hole magneto-plasma, surprisingly, shows excitonic character in the magnetic field dependence of its emission energy.

3.1 Interband Transitions of Quasi-2D Electron-Hole Pairs in a Magnetic Field

In two-dimensional semiconductor samples, a perpendicular magnetic field quantizes the electronic states of the conduction and valence band such that the 2D density of states begins to show a zero dimensional density of states where the stairstep profile becomes a series of delta functions. Many interesting physical phenomena can be studied under this full quantization condition.

3.1.1 Interband Absorption in Semiconductor Quantum Wells

When light is incident on a semiconductor, electrons in the valence band can absorb photons and transition to the conduction band to form electron-hole pairs if the photon energy is greater than the band gap. Transitions between the conduction band and valence band are referred to as interband transitions. Ignoring excitonic effects, the absorption coefficient is proportional to the joint density of states. In the case of 3D or bulk semiconductors, the absorption coefficient is given, by

$$\alpha(\hbar\omega) = \frac{4\pi^2 e^2 \hbar}{m^2 c\eta} \frac{1}{\hbar\omega} |\mathbf{a} \cdot \mathbf{p}_{if}|^2 N(\hbar\omega) \tag{3.1}$$

where

$$N(\hbar\omega) = \frac{\sqrt{2}(\mu)^{\frac{3}{2}}(\hbar\omega - E_g)^{\frac{1}{2}}}{\pi^2\hbar^3} \tag{3.2}$$

is the 3D density of states for parabolic bands, η is the index of refraction, μ is the reduced effective mass in Eq. 3.12, E_g is the band gap, m is the free electron mass, $\hbar\omega$ is the photon energy,

$$|\mathbf{a} \cdot \mathbf{p}_{if}|^2 = \left| \int \psi_f^* p_a \psi_i e^{i\mathbf{q}\cdot\mathbf{r}} d^3r \right|^2 \tag{3.3}$$

is the matrix element where ψ_i and ψ_f are the wavefunctions for the initial and final states, and p_a is the momentum component along the polarization direction. If $\hbar\omega < E_g$, then $\alpha(\hbar\omega) = 0$. In the case of 2D semiconductor structures, the absorption coefficient is given by

$$\alpha(\hbar\omega) = \frac{4\pi^2 e^2 \hbar}{m^2 c\eta} \frac{1}{\hbar\omega} |\mathbf{a} \cdot \mathbf{p}_{if}|^2 \frac{N_{2D}(\hbar\omega)}{W} \sum_{n,m} f_{nm}\theta(E_{nm} - \hbar\omega) \tag{3.4}$$

where

$$N_{2D} = \frac{\mu}{\pi\hbar^2} \tag{3.5}$$

is the 2D density of states for parabolic bands, θ is the Heaviside step function which is 0 for negative arguments and 1 for positive arguments, f_{nm} represents the overlap between the n and m subband wavefuctions, and W is the transition rate between the initial and final states. The function, f_{nm}, is close to 1 for $n = m$ and zero, otherwise [14]. Figure 3.1 shows the density of states as a function of $E = \hbar\omega - E_g$

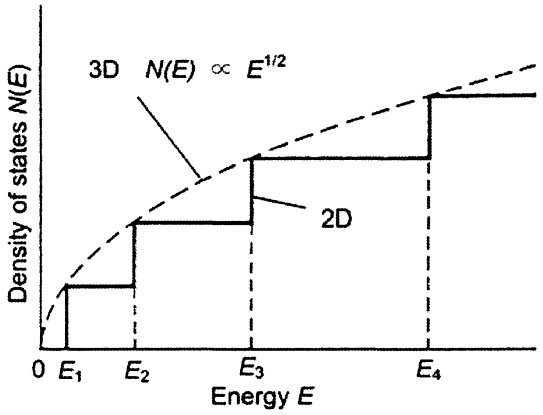

Figure 3.1 : Comparison of the 2D and 3D density of states [1].

and $E = E_{nm} - \hbar\omega$ for the case of 3D and 2D, respectively. The 3D density of states shows a $\sqrt{E}$ energy dependence while the 2D density of states shows a stairstep energy dependence where each step occurs at the location of a subband transition. Because quantum well samples are two dimensional systems, the direct allowed interband transitions are between the subbands in the conduction and valence bands with the same quantum number after evaluation of the electron and hole wavefunction overlap integrals [26].

3.1.2 Excitonic Effects

If the Coulomb interaction is taken into consideration, bound states of the electron-hole pair arise which are analogous to the bound states of the hydrogen atom. A photon with slightly less energy than the band gap can be absorbed to create an exciton, a bound electron-hole pair. This modifies the absorption coefficient of the semiconductor by adding a peak in the profile at slightly less energy than the band gap. The difference in energy of the exciton and the band gap is called the exciton binding energy.

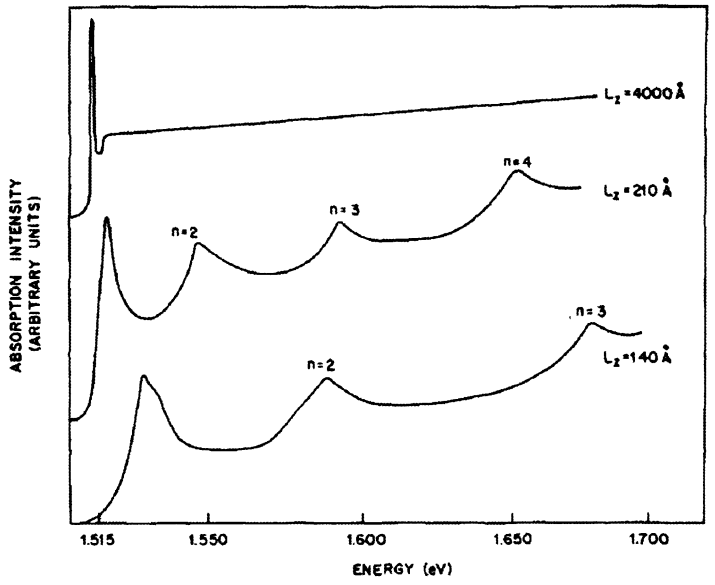

Figure 3.2 : Absorption from GaAs quantum wells as a function of well thickness. There is a transition from 3D behavior to 2D behavior when reducing the quantum well thickness. For smaller thicknesses, multiple exciton peaks form and the continuum absorption profile approaches a stairstep profile [2].

Figure 3.2 shows experimental results for GaAs quantum wells with varied well thickness. It is clear that the absorption profile shows a transition from 3D behavior to 2D behavior as the well thickness decreases. In the sample with large quantum well

thickness, there is a single exciton peak just below the band gap energy and above that energy the continuum absorption increases. As the thickness of the quantum well decreases, multiple exciton peaks form and the continuum absorption profile approaches a stairstep profile.

3.1.3 Landau Levels in Semiconductor Quantum Wells

For a two-dimensional electron system, the component of a magnetic field perpendicular to the layer quantizes the orbital motion of the electron. The energy spectrum of the electron is quantized into Landau levels (LLs) at energies

$$E_N = \left(N + \frac{1}{2}\right)\hbar\omega_c \tag{3.6}$$

where

$$\omega_c = \frac{eB}{m^*} \tag{3.7}$$

is the cyclotron frequency, N=0,1,2... is the LL index, m^* is the effective mass of the electron, and B is the magnetic field. The density of states for the 2D electrons becomes a series of delta functions, and the number of states of each LL is given by

$$N_{2D}(B) = \frac{e}{h}B \tag{3.8}$$

When a magnetic field is applied perpendicular to a semiconductor quantum well, each valence and conduction subband becomes fully quantized to form a series of LLs. Transitions between the conduction and valence band LLs are allowed between LLs with the same, $N = M$, LL index [1]. The energy separation for these transitions, ignoring excitonic effects, is given by

$$E_N = E_g^* + \left(N + \frac{1}{2}\right)\hbar\omega_c \tag{3.9}$$

where

$$E_g^* = E_g + E_e(n_s) + E_h(n_s) \tag{3.10}$$

is the effective band gap,

$$\omega_c = \frac{eB}{\mu} \tag{3.11}$$

is the cyclotron frequency, E_g is the band gap of the well, and $E_{e,h}(n_s)$ is the energy of the n_s-th conduction or valence subband. The reduced effective mass of the electron-hole pair, μ, is defined by

$$\frac{1}{\mu} = \frac{1}{m_e^*} + \frac{1}{m_h^*} \tag{3.12}$$

where m_e^* is the effective mass of the electron and m_h^* is the effective mass of the hole.

The magnetic field dependence for the magneto-exciton energy can be approximated in the low and high magnetic field limits using perturbation theory. In the low magnetic field limit, when the Coulomb interaction is the dominant term in the Hamiltonian and the magnetic field is treated as a perturbation, the magnetic field dependence is given by

$$E_N = E_g^* - \frac{Ry^*}{(N+\frac{1}{2})^2} + \frac{5}{8}\left(N+\frac{1}{2}\right)^2\left[\left(N+\frac{1}{2}\right)^2 + \frac{7}{20}\right]\frac{(\hbar\omega_c)^2}{Ry^*} \tag{3.13}$$

where

$$Ry^* = \frac{\mu e^4}{32\pi^2\epsilon^2\hbar^2} \tag{3.14}$$

is the exciton effective Rydberg energy [27]. The third term in Equation 3.13 is the diamagnetic shift, which gives the transition energy a quadratic dependence on magnetic field. The orbit of the bound electron-hole pair creates an induced magnetic field that partially cancels the applied magnetic field. This is the origin of the diamagnetic shift. In the high magnetic field limit, the Landau quantization begins to dominate and the Coulomb interaction is treated as a perturbation. In this limit, the

magnetic field dependence is given by

$$E_N = E_g^* + \left(N + \frac{1}{2}\right)\hbar\omega_c - \alpha_N(\hbar\omega_c Ry^*)^{\frac{1}{2}} \tag{3.15}$$

where α_N are numerical coefficients on the order of 1 [28]. There is no analytic method for combining these two regimes.

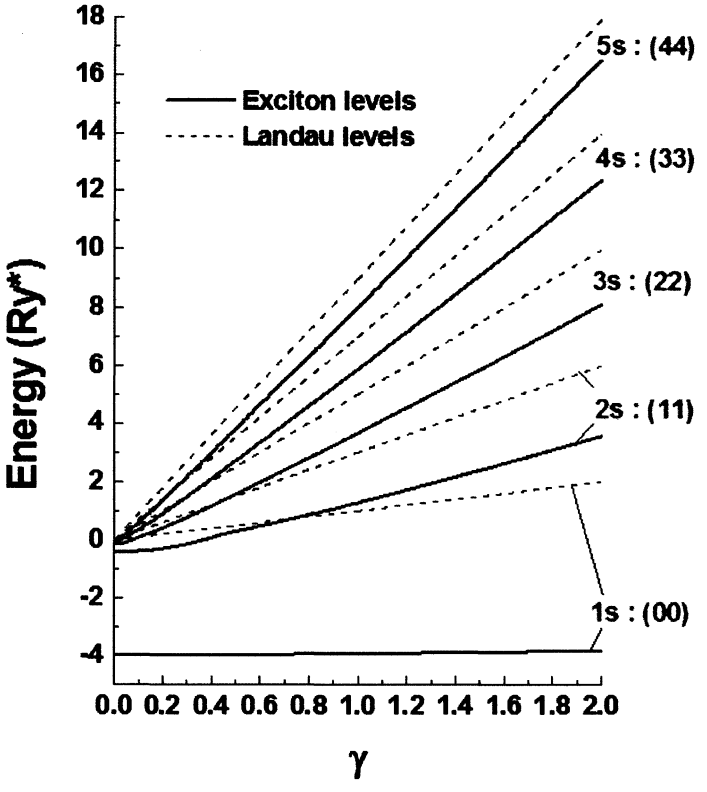

Figure 3.3 : Comparison between the energy of magneto-exciton levels and LLs as a function of γ, a parameter that compares the magnetic energy to the Coulomb energy. The exciton levels show the diamagnetic shift while the LLs show a linear magnetic field dependence.

Figure 3.3 shows the energy in exciton effective Rydberg as a function of γ,

$$\gamma = \frac{\frac{\hbar\omega_c}{2}}{Ry^*} \tag{3.16}$$

where γ is a parameter that compares the magnetic energy to the Coulomb energy for the magneto-exciton levels and LLs. In this figure, the hydrogenic exciton levels and the LLs are labeled $1s$,$2s$,$3s$,... and 00,11,22,..., respectively. In this study, we will use the Landau notation (N,M) to specify each 2D magneto-excitonic state instead of the low field notation (n,m). Unlike in 3D semiconductor systems, in the case of two dimensions, there is a one-to-one correspondence between the two descriptions and this correspondence is given by $n = N + 1$ and $m = N - M$ [28].

3.1.4 Regimes of Electron-Hole Pairs

Electron-hole pairs show different characteristics depending on their density. In the low-density regime, the electron and hole are bound to one another via the Coulomb interaction to form an exciton. With increasing density, when the Bohr radius becomes comparable to the interexciton distance, a Mott transition will occur, transforming an insulating excitonic gas into a metallic electron-hole plasma where the electrons and holes are no longer bound to another, i.e., the exciton binding energy is zero [29].

Figure 3.4 shows a schematic diagram for electron-hole pairs as a function of pair density and magnetic field. In the low-density regime, excitons become magneto-excitons with emission energies given by Equations 3.13 and 3.15 as the applied magnetic field increases. In the high-density regime, the electron-hole plasma becomes an electron-hole magnetoplasma with magnetic field dependent emission energies given by Equation 3.9. In this work, we are primarily interested in the high-density, high-magnetic field regime indicated by the question mark.

For 2D electron-hole systems in strong perpendicular magnetic fields, theoretical studies have shown that there exists a "hidden symmetry" for ν_e,$\nu_h \leq 2$ (where ν_e,ν_h

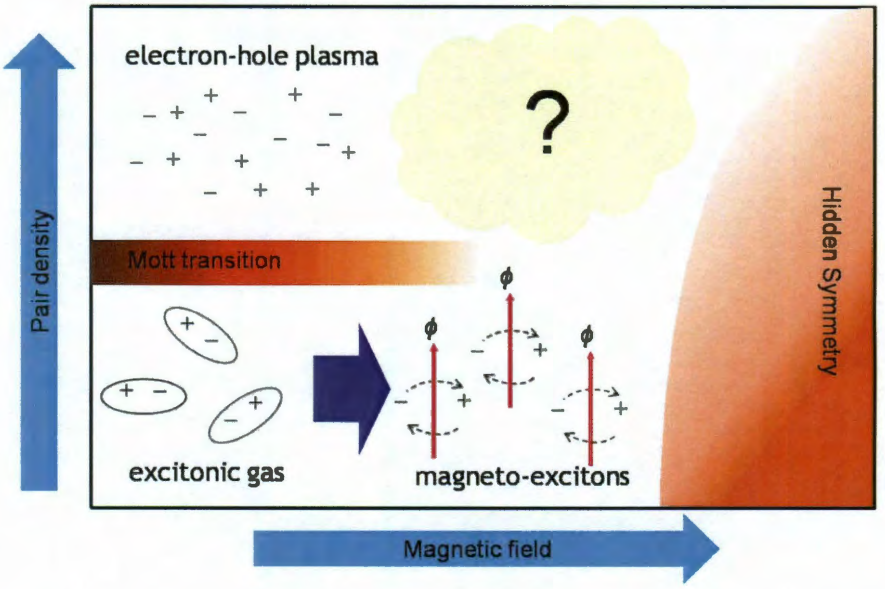

Figure 3.4 : Different regimes of electron-hole pairs as a function of pair density and magnetic field. With increasing electron-hole pair density, an excitonic gas experiences a Mott transition to become an electron-hole plasma. With increasing magnetic field, an excitonic gas becomes magneto-excitons. We have investigated the high magnetic field and high pair density regime. Adapted from [3].

are the electron and hole filling factors), which leads to an exact cancelation of interexciton Coulomb interactions [30–32]. The filling factor, ν, is equal to the number of LLs that are filled. The consequence of this "hidden symmetry" is that an electron-hole magneto-plasma can transform back into magneto-excitons with increasing magnetic field, reversing the effect of a Mott transition. The experimental evidence for this "hidden symmetry" has been shown as a change from a linear magnetic field dependence for emission energies to a quadratic dependence at ν_e,$\nu_h = 2$ [31].

3.2 Experimental Methods

3.2.1 $In_{0.2}Ga_{0.8}As$ Quantum Well Sample

The $In_{0.2}Ga_{0.8}As$ multiple quantum well sample used in this study consists of a GaAs buffer layer followed by 15 layers of 8 nm $In_{0.2}Ga_{0.8}As$ quantum well separated by 15 nm GaAs barriers with a 10 nm GaAs cap layer. Because the lattice constant of the $In_{0.2}Ga_{0.8}As$ quantum well is larger than the surrounding GaAs barriers, there is compressive strain induced that shifts the band gap energies and induces a large valence band offset. Most importantly, the light hole (LH) energy relative to the heavy hole (HH) energy is lowered to reduce the hole-level coupling and its repulsive interaction between LH and HH subbands. Therefore, this sample minimizes the effects of valence band complexities in order to obtain discrete optical spectra of the HH and LH excitons, especially, in the high magnetic field regime [33]. Also, the substrate, GaAs, is transparent in the energy range where these interband transitions occur, so there is no need to remove the substrate via etching in order to measure absorption or photoluminescence.

Figure 3.5 shows the absorption profile of this $In_{0.2}Ga_{0.8}As$ quantum well sample. Here, we see the large separation of the HH and LH in the valence band by looking at the interband transitions from the HH and LH subbands to the lowest subband in the conduction band along with the exciton resonant transitions.

3.2.2 Experimental Setup

Our magneto-absorption and magneto-photoluminescence measurements were done in the Ultrafast Optics facility at the National High Magnetic Field Laboratory in Tallahassee, Florida. We used the 17.5 Tesla superconducting magnet in cell 3 (SCM3)

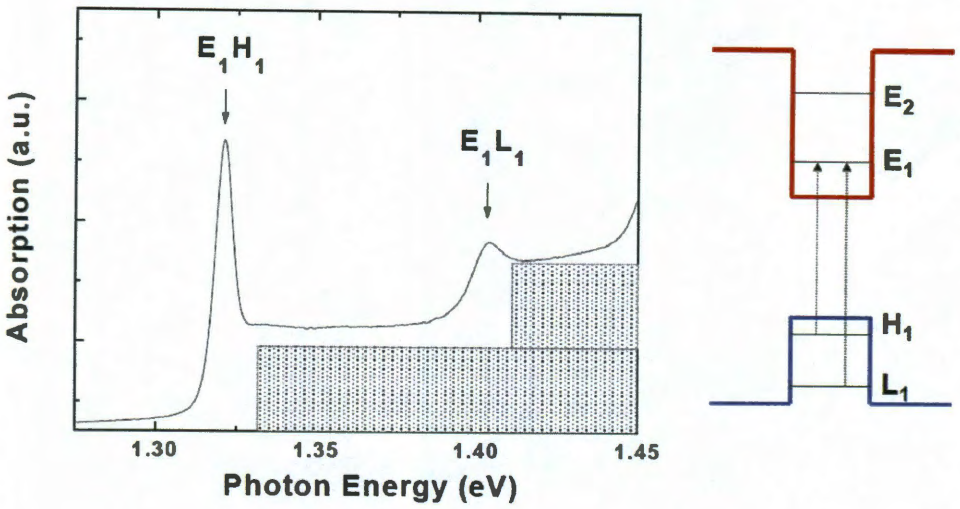

Figure 3.5 : Absorption profile of the $In_{0.2}Ga_{0.8}As$ quantum well sample studied in this work. The E_1-H_1 and E_1-L_1 exciton transitions are visible as well as the continuum absorption for the first subbands.

of the Magnet Lab. SCM3 is a cold bore system with bore radius of 47 mm and is capable of measurements from 4 to 300 K. Cell 3 houses a Coherent Legend regeneratively amplified laser that can produce 2.5 mJ, 800 nm, and 150 fs pulses at 1 kHz repetition rate and pumps a Light Conversion TOPAS-800 OPA to provide a tunable source of pulsed radiation from the UV up to 20 μm.

To prepare the sample for measurements inside SCM3, we, first, mount the sample and a μ-prism (1 mm^2 area) on a sapphire window where the μ-prism is placed at the edge of the sample to redirect the in-plane emission. The sample and μ-prism are secured to the sapphire window using UV epoxy that is transparent to near-IR radiation. The probe has two 0.6 mm core diameter multimode optical fibers that extend down the probe such that the bare ends of the fibers are positioned at two holes in the copper end, one in the center and one 2 mm to the side. Then, the prepared sample is secured to the copper end of the probe using 3 clamps and a dab

of GE varnish such that the center of the sample is positioned over the center fiber and the μ-prism is positioned over the edge fiber. Figure 3.6 shows a diagram of the

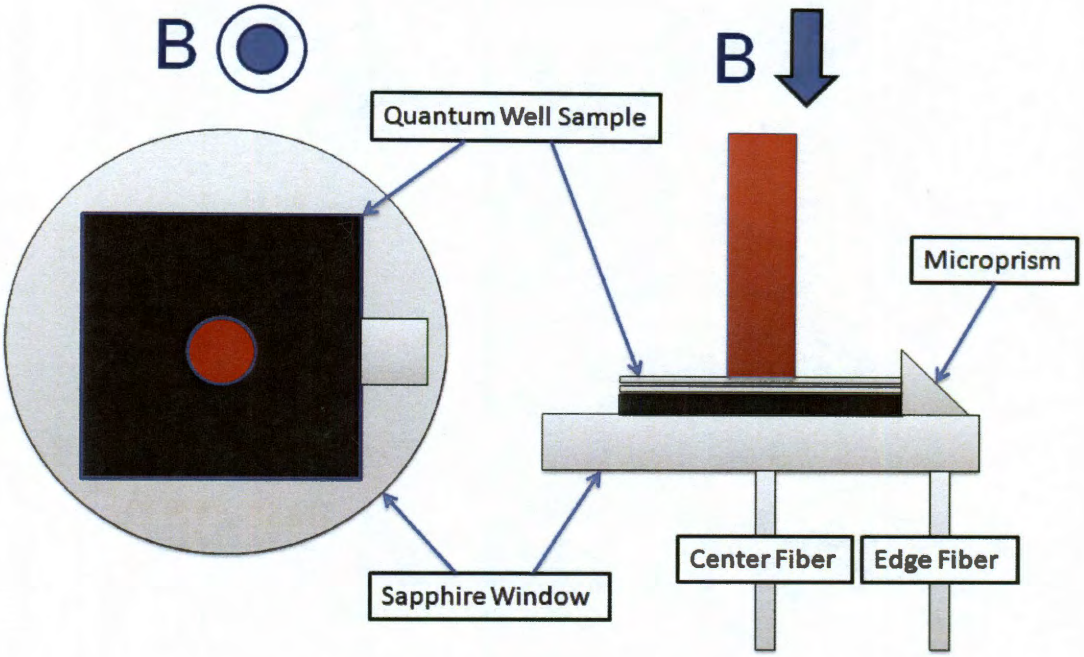

Figure 3.6 : A quantum well sample is attached to a sapphire window, and a μ-prism is attached to redirect the in-plane emission into an edge-collection fiber. The experiment is performed in the Faraday geometry where the magnetic field is parallel to the incident light.

prepared sample and experimental geometry. The probe is lowered down SCM3 such that the sample is placed at the point in the magnet with highest magnetic field. The experiment is done in the Faraday geometry where the incident light is parallel to the magnetic field and perpendicular to the quantum wells. Two fibers, referred to as the center and edge, are SMA connectorized at the end of the fibers outside of the magnet so that we could measure their collected light with a spectrometer, streak camera, or fast photodiode.

For low and high excitation photoluminescence (PL) studies, a 25-mW He-Ne laser

and the amplified Ti:Sapphire laser beams were introduced through a CaF_2 at the bottom of the magnet bore. A quartz-tungsten halogen lamp was used for white-light transmission measurements. We used a 1 m focal length McPherson spectrometer to measure the transmission and PL as a function of magnetic field. For nonlinear PL, pulse energies up to 10 μJ were focused to a 0.5 mm diameter with a 1 m spherical lens to create a pump fluence of $\sim$5 mJ/cm^2.

3.3 Experimental Results

Figure 3.7 shows the magnetic field dependence of the emission and absorption spectra for the $In_{0.2}Ga_{0.8}As$ quantum well sample. The absorption spectra, at zero field, shows a stairstep like profile with peaks at the E_1-H_1, E_1-L_1, and E_2-H_2 excitons at energies of 1.325, 1.40, and 1.45 eV, respectively. Each excitonic absorption peak evolves into a series of sharp LLs with increasing magnetic field. In this study, we focus only on the splitting of the E_1-H_1 exciton absorption peak and PL emission into the 00, 11, 22, ... LLs. The low-density (He-Ne excitation), center-collected PL spectra show a single peak with increasing intensity and slight diamagnetic shift with increasing magnetic field. The high-density (amplified Ti:Sapphire excitation), edge-collected PL shows emission from the E_1-H_1 exciton evolve into a spectacular series of sharp peaks with increasing separation as the magnetic field increases.

Figure 3.8 shows the power dependence of the high-density PL at 0 and 17 Tesla. The 0 field spectra show significant broadening and emission from the continuum on the high-energy side of the peak with increasing power. The 17 Tesla spectrum shows a single peak at the lowest pump power. With increasing power, there is emission from multiple peaks that increase in intensity but shows no sign of broadening or a shift in peak position.

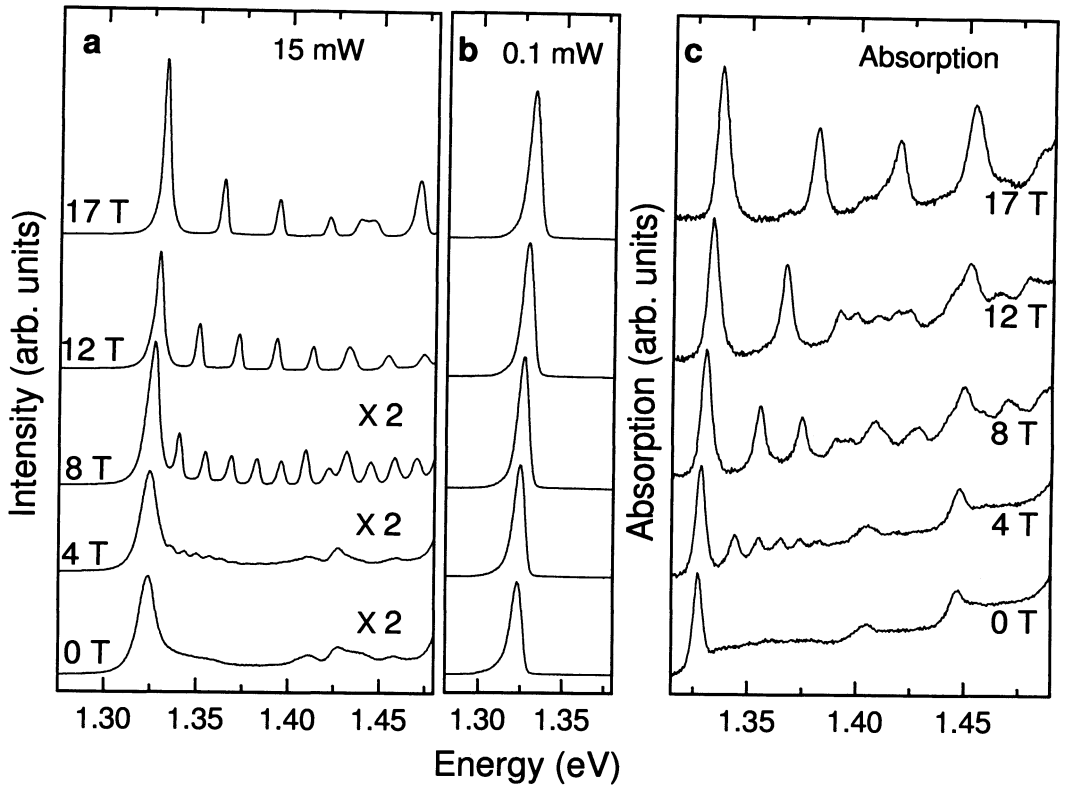

Figure 3.7 : Side by side comparison of nonlinear photoluminescence (**a**), linear photoluminescence (**b**), and absorption spectra (**c**) for different magnetic fields. The nonlinear photoluminescence measurements show bright emission from multiple LLs emerge with increasing magnetic field. The linear photoluminescence data shows a small diamagnetic shift with increasing magnetic field. The absorption profile shows 2D absorption features evolve into a series of LLs [3].

The Landau fan diagrams in Figure 3.9 shows the results of fitting the absorption, and nonlinear PL to obtain the center peak energy as a function of magnetic field. Because the LL splitting is not clear, we could not obtain the peak positions of the higher LLs at small magnetic fields. Only the peak position of the 00LL could be obtained at all magnetic fields. After finding the peak energy for each transition as a function of magnetic field, the result was then fit to a Padé approximation for an ideal 2D hydrogen atom in arbitrarily strong magnetic field for both the absorption and

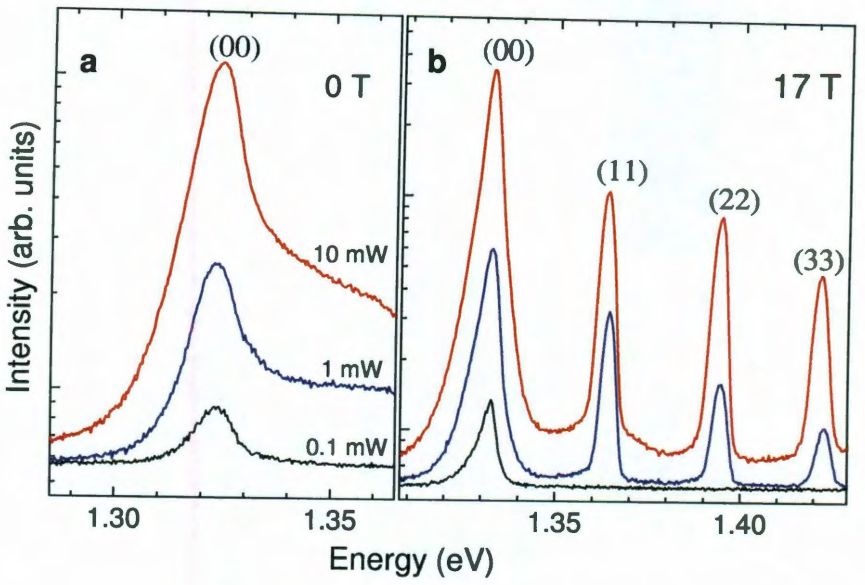

Figure 3.8 : Nonlinear photoluminescence for different excitation powers at 0 (**a**) and 17 Tesla (**b**). The 0 Tesla data shows broadening and emission from the continuum on the high-energy side of the E_1-H_1 exciton peak with increasing power. The 17 Tesla data shows no sign of broadening with increasing power [3].

nonlinear PL data [28]. By extrapolating the higher LLs back to zero magnetic field, one can determine the exciton binding energy. Magnetic field dependent absorption measurements have proved useful for finding the exciton binding energy for many semiconductor materials [1]. The absorption results show the higher LLs converging to band gap for the $In_{0.2}Ga_{0.8}As$ quantum well at zero magnetic field. The difference between the band gap and the E_1-H_1 transition is the exciton binding energy of 13.6 meV. The nonlinear PL results show all LLs converging to the same point, showing zero exciton binding energy.

Figure 3.10 shows the result of numerically solving the Schrödinger equation for a system including an electron and heavy hole to get the magnetic field dependence of the absorption as well as the nonlinear PL peaks. The Hamiltonian includes the quantum well confinement in the growth direction, the interaction with magnetic

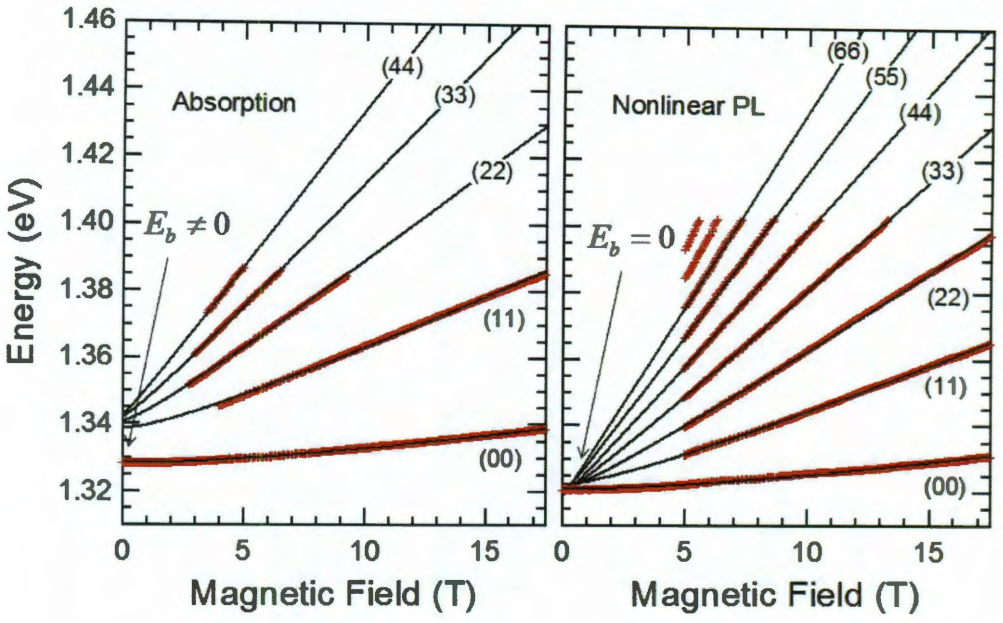

Figure 3.9 : A side by side comparison of absorption and nonlinear photoluminescence Landau fan diagrams shows the electron-hole pair energies as a function of magnetic field. The absorption diagram shows a diamagnetic shift, and the extrapolation of the fit shows the higher LLs approach the effective band gap of the well. The difference between the effective band gap and the 00LL at zero magnetic field corresponds to a finite binding energy. The nonlinear photoluminescence diagram shows all LLs converge to the same point at zero magnetic field indicating zero exciton binding energy but the magnetic field dependence of the 00LL shows excitonic character at all magnetic fields.

field, and the Coulomb interaction between them. For the nonlinear PL data, the band gap was treated as a fitting parameter to allow for its renormalization [3]. The results of these calculations show excellent agreement with the experimental data.

3.4 Discussion

Our results show that at zero magnetic field, increasing the density of excitons leads to a Mott transition to an electron-hole plasma because all of the LLs converge to

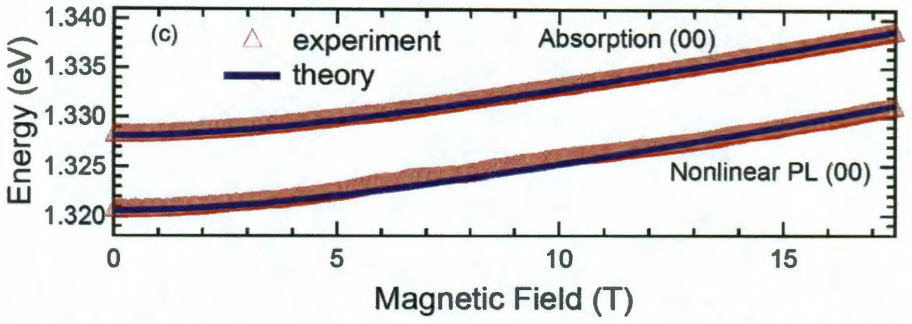

Figure 3.10 : A close up comparison of the absorption and nonlinear photoluminescence experimental result and numerical calculation for the 00LL. The calculation solves the Schrödinger equation for a system including only an electron and heavy hole to get the magnetic field dependence. Adapted from [3].

the same point on the Landau fan diagram for our high-density measurements. A quick, rough estimate of the electron-hole densities can be made by using Eq. 3.8 for the density per full LL and multiplying it by the number of full LLs emitting radiation for a given magnetic field. At 17 Tesla, the density can be calculated to be $\sim 2.5 \times 10^{12}$ cm^{-2}. Figure 3.8 shows 4 full LLs emitting at 1 mW, and we used powers up to 10 mW so our excitation power should create electron-hole densities approaching 10^{14} cm^{-2}. The magnetic field dependence of the emission energy for the high-density electron-hole magnetoplasma shows the clear excitonic character of a diamagnetic shift, it can be fitted well to the Padé approximation for an ideal 2D hydrogen atom in arbitrarily strong magnetic field, and it can be solved numerically for a system including only an electron and heavy hole. These results show that, at any finite magnet field, an electron-hole magnetoplasma can emit as a gas of non-interacting excitons.

Our results are different from previous studies [34] that do not show this behavior because we used an intense pulsed laser at high pump fluences to create population-

inverted electron-hole pairs. In this case, spontaneous emission can be amplified by stimulating the emission of other population-inverted electron-hole pairs that provide gain to the system. This gain is dramatically enhanced when the recombining electron-hole pair spatially overlap to form a neutral two particle exciton state. Although the initial spontaneous emission is spread over a broader range of energies corresponding to the transitions between many-particle states of the system, the stimulated emission is concentrated within a narrow region near the peak of the gain at the single-exciton energy [3]. We observe single-exciton emission peaks precisely because this stimulated emission dominates the spectra.

Because there are many peaks in the nonlinear PL spectrum, we can conclude that our electron and hole filling factors are greater than 2 which violates the theoretically predicted and experimentally verified constraint on the applicability of the "hidden symmetry" that prevents all interexciton interactions. Therefore, our results provide an extension to this concept as our range of magnetic field and density go well beyond the ranges where it has been shown to be valid.

3.5 Conclusion

We measured absorption along with low- and high-density excitation PL in order to investigate the magnetic field dependence of the energies of low- and high-density electron-holes pairs in an $In_{0.2}Ga_{0.8}As$ multiple quantum well sample at 5 K. These results show that high-density electron-hole pairs, in the presence of gain and a finite magnetic field, can show emission properties that are excitonic despite the fact that their densities exceed the Mott density.

Chapter 4

Superfluorescence from Quantum Wells in High Magnetic Field

The phenomena of superradiance (SR) was originally proposed by Robert Dicke in his seminal paper, "Coherence in Spontaneous Radiation Processes" [18] to describe a class of radiation where the recombination rate of a single inverted dipole is enhanced due to the presence of other two-level dipoles nearby. SF is a particular example of superradiant emission where an ensemble of population-inverted two-level dipoles is prepared with an incoherent preparation method to ensure that the system possesses no coherent macroscopic polarization followed by the spontaneous development of macroscopic polarization and a burst of radiation completely reversing the population inversion. SF has been extensively experimentally measured in atomic and molecular systems but not in condensed matter systems where ultrafast scattering phenomena typically destroys such coherence. Here, we present the first direct observation of SF in a semiconductor quantum well sample in a magnetic field.

4.1 Previous Studies of Superfluorescence

4.1.1 Theoretical Development

Dicke's original paper theoretically explored the situation where a large number of molecules, N, as a system of two-level dipoles, contained in a small volume are radiating with a high degree of coherence between the individual dipoles. Previously, the

usual treatment of spontaneous emission assumed that the gas of molecules radiate independently of one another with radiative intensity proportional to N. He was able to show that the intensity of radiative power for this coherently radiating gas of molecules could be proportional to N^2 [18]. Furthermore, he was able to show that the coherent emission from this gas could radiate for a duration, $t_p \propto T_1/N$, rather than an exponential decay with lifetime, T_1, independent of the number of molecules. He referred to this type of emission as 'super-radiant' emission. He also pointed out that if the N molecules were incoherently prepared with population inversion in a volume small compared to the wavelength cubed, the molecules will begin to radiate spontaneously and incoherently but, then, the spontaneous emission from any one molecule or small fraction of molecules will cause the inverted system to develop a very large coherent macroscopic polarization, and, after a certain delay time, will emit a pulse of radiation with duration, $t_p \propto T_1/N$, and intensity proportional to N^2 [35].

The emission process of incoherently prepared SR can be solved classically, and the dynamics can be simply described using the Bloch sphere where the equation for the polar angle, θ, is the classical equation for an overdamped pendulum [18,36]. Figure 4.1 shows the Bloch sphere where the Bloch vector represents the sum of all of the N dipoles in a small volume. The north pole represents all of the dipoles in the excited state, and the south pole represents all of the dipoles in the ground state. Equation 4.1 is the overdamped pendulum equation for the polar angle of the Bloch vector.

$$\frac{d\theta}{dt} = -\frac{N+1}{2T_1}\sin\theta \tag{4.1}$$

Initially, the Bloch vector points up, $\theta = \pi$, indicating that all of the dipoles are in the excited state. This initial state is stable, meaning that all of the dipoles remain in the excited state, but, if there is an initial tip of the Bloch vector, it continues to

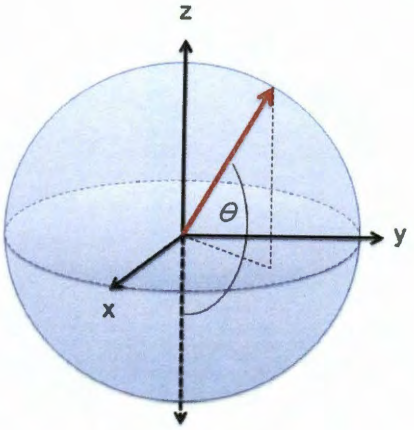

Figure 4.1 : Bloch sphere representation of SR emission dynamics. The polar angle of the Bloch vector obeys the overdamped pendulum equation. Initially, $\theta = \pi$ indicates all of the dipoles are in the stable excited state. After an initial tip of the Bloch vector, it continues to move away from the north pole through the equator and completely stops at the south pole, indicating all of the dipoles are in the ground state and all of the energy has been emitted as light.

move away from the north pole through the equator and, finally, completely stopping at the south pole when $\theta = 0$, indicating that all of the dipoles are in the ground state and all of the energy has been emitted as light. This classical description is adequate to describe the emission process but only after an initial tip of the Bloch vector. A full quantum mechanical treatment is required to describe the initial tipping of the Bloch vector from the stable north pole. The first few photons that are emitted from the initially inverted dipoles arise as quantum noise. These photons cause the inverted system to develop a large coherent macroscopic polarization and the radiated pulse from this macroscopic polarization maintains characteristics that result from amplified quantum fluctuations [37, 38].

The restriction of Dicke's incoherently prepared SR that requires the inverted two-level dipoles occupy a volume small compared to the wavelength cubed is ex-

perimentally difficult to obtain for optical systems. However, there is a more general situation in which the large number of inverted dipoles can occupy an extended region of space such as a long, thin cylindrical region with Fresnel number,

$$F = \frac{A}{\lambda L} \approx 1 \tag{4.2}$$

where A is the area of the end of the cylinder, λ is the wavelength of the emission, and L is the length of the cylinder. SR in an extended region of space after preparing a population inversion with no initial coherence is referred to as SF. The experimental features of SF will be an intense burst of coherent radiation coming out in a narrow cone from each end of the cylinder with intensity proportional to N^2, pulse duration, $t_p \propto T_1/N$, and a delay following the initial incoherent preparation of inverted two-level dipoles. Furthermore, because the emission is initiated by random spontaneous emission, there will be shot-to-shot fluctuations in the time delay and direction of SF pulses [35]. Amplified spontaneous emission is spontaneous emission that becomes optically amplified by stimulated emission in a gain medium. In experiments that excite an extended region of space to create a large population of inverted dipoles, amplified spontaneous emission (ASE) is often observed in addition to the observation of SF making it sometimes difficult to clearly distinguish SF.

4.1.2 Previous Evidence for Superfluorescence from Atomic Systems

SR and SF have been observed in atomic and molecular gases. The first experimental study and observation of SF in the optical range was done by Skribanowitz et al. in 1973 using a HF gas at millitorr pressures [4]. Here, the gas was pumped using a HF laser with pulse widths of 200-400 ns to create nearly complete population inversion between adjacent rotational transitions in the 50-250 μm range. The experimenters

took precautions such that the lower photon energy emission from this laser did not enter into the sample cell. Figure 4.2 shows the experimental and theoretical results for the case of 84 μm emission pumped by a 3 μm pulse at intensity of 1 kW/cm^2. The

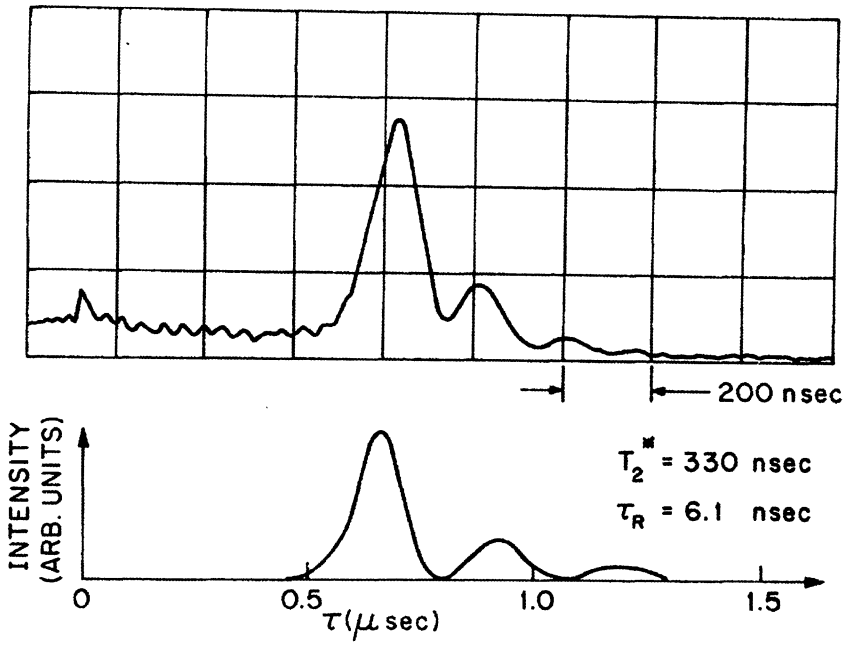

Figure 4.2 : Oscilloscope trace (**top**) and theoretical result (**bottom**) of SF emission from a HF gas at millitorr pressures. The initial bump in the oscilloscope trace was the pump laser pulse, attenuated. There was a delay between the pump pulse and the SF pulse [4].

emission was measured with a helium cooled InGe detector with a fast preamplifier and a pulse amplifier for an overall rise time of 10 ns for the detection system. The small peak on the oscilloscope trace at t=0 is the pump pulse, highly attenuated. The theoretical result, shown in the lower panel of Figure 4.2, is consistent with the experimental result showing a pulse of radiation with some delay time after the pump pulse. Further measurements showed that decreasing the pressure or decreasing the pump intensity resulted in longer delays between the pump and pulsed emission along

with a broadening of the pulse [4].

The second experimental study and observation of SF in the optical range was done studying cascading transitions in atomic sodium by Gross et al. in 1976 [5]. Here, they used two tunable dye lasers, $\lambda_1 = 589$ nm and $\lambda_2 = 616$ nm, with 2 ns pulse width pumped by the same N_2 laser in order to populate the $5S_{\frac{1}{2}}$ state. Figure 4.3 shows (**a**) the transitions and (**b**) the basic experimental setup. Figure 4.4 shows

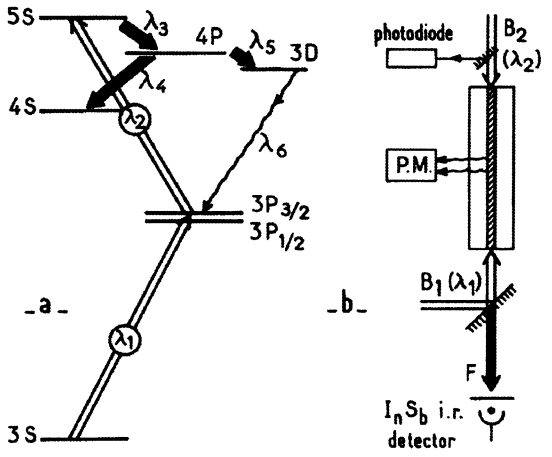

Figure 4.3 : Transition diagram (**a**) and experimental setup (**b**) for measuring SF from cascading transitions in atomic sodium. Two pulsed dye lasers were used to populate the 5S state. The emission from the 5S-4P and 4P-4S transitions were measured [5].

the signal collected by a fast InSb detector measured with a fast transient recorder after selectively filtering the various transitions with the appropriate optical filter. The results show (**a**) the pump pulse, (**b**) a pulse from the 5S-4P transition for two different pump intensities, and (**c**) a pulse from the 4P-4S transition. This data shows clear delays between the time the population inversion begins and the SF pulse that develops for multiple transitions. These observations were the first evidence of SF in the near-IR [5].

Later, single-pulse observations of SF were made by pumping cesium with a dye

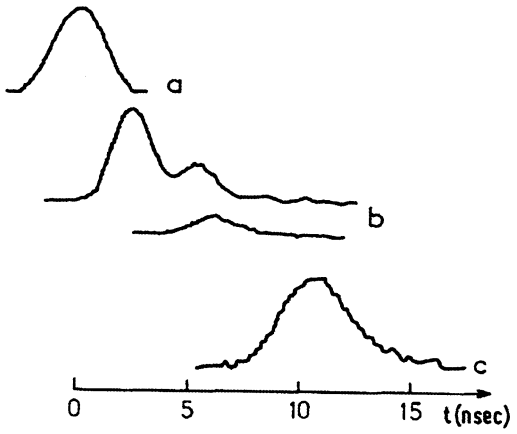

Figure 4.4 : SF pulses from cascading transitions in atomic sodium after the pump pulse (**a**). Delayed pulses were observed for the 5S-4P transition (**b**) at high and low pump intensity and for the 4P-4S transition (**c**) [5].

laser with 2 ns pulse width and 455 nm by Gibbs et al. in 1977 [6]. However, the experimental results were not in good quantitative agreement with the current theory at the time. The difference between this experiment and previous ones was that a carefully prepared transition in Cs could ensure almost ideal conditions for observing "pure" SF as described by Bonifacio and Lugiato [36]. The previous experiments could not satisfy the stringent conditions so they could not answer the question whether single pulse emission could be observed. Figure 4.5 shows the results as a function of density. At lower densities, single-pulse emission is demonstrated. At the highest density, the authors mention that multiple pulses occur with shapes that fluctuate greatly from pulse to pulse [6]. This may have been evidence of the random nature of SF.

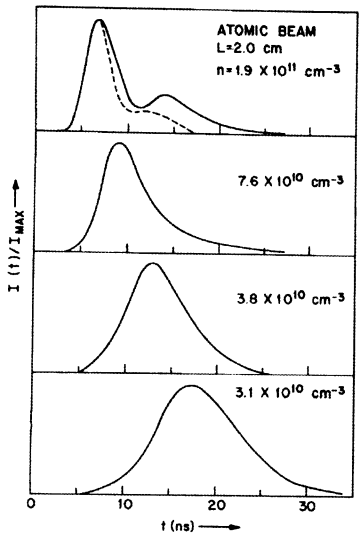

Figure 4.5 : Single pulse SF pulses from cesium at lower pump intensities (**lower traces**) and multiple pulses with pulse to pulse fluctuations in shape at the highest pump intensity (**top trace**) [6].

4.1.3 Theory for Superfluorescence in Quantum Wells

It was proposed by Belyanin et al. that SF was possible in semiconductor quantum wells in high magnetic fields [39]. To observe SF from a system of electron-hole pairs in a semiconductor quantum well, the cooperative frequency,

$$\omega_c = \sqrt{\frac{8\pi^2 d^2 N \Gamma_c}{\hbar n^2 \lambda L_{QW}}} \tag{4.3}$$

which is the key parameter that determines the coupling strength between the field and the optical polarization, must be greater than $2/T_2$, where d is the transition dipole moment, N is the 2D electron-hole density, Γ_c is the overlap of radiation with the quantum wells, c is the speed of light, n is the refractive index, λ is the wavelength, L_{QW} is the total width of the quantum wells, and T_2 is the homogeneous phase relaxation time (dephasing time of optical polarization). In semiconductors, T_2 is typically 1-10 ps, making it difficult to satisfy the above condition. By placing

a semiconductor quantum well in a high magnetic field, the density of states will be greatly increased due to the Landau quantization. Furthermore, the filling of all the lower LLs should also increase T_2, making it possible to achieve the threshold for SF [9].

Under the ideal conditions for SF, the pulse duration should scale as

$$\tau_{SF} \propto \frac{1}{\omega_c} \propto N^{-\frac{1}{2}} \tag{4.4}$$

and the peak intensity scales as

$$I_{SF} \propto \frac{\hbar\omega N}{\tau_{SF}} \propto N^{\frac{3}{2}} \propto B^{\frac{3}{2}} \tag{4.5}$$

where B is the magnetic field applied perpendicular to the quantum wells. The theoretically predicted coherence length for SF emission in quantum wells is ~0.5 mm.

Figure 4.6 shows theoretical results from our collaborators for the exciton occupation and intensity of SF as a function of time [7]. These results show a sudden

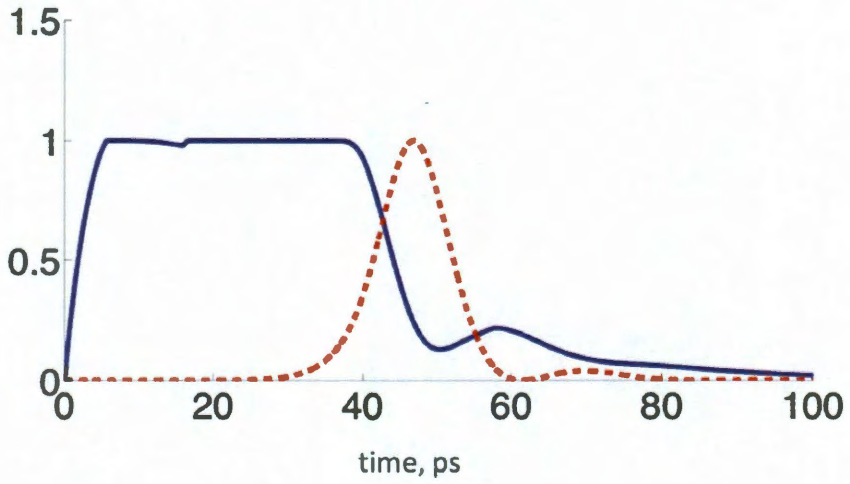

Figure 4.6 : Occupation number of excitons on 22LL (**blue line**) and intensity of SF emission (**dashed red line**) as a function of time since the pump pulse [7].

depopulation of the 22LL state and the corresponding SF pulse at around 50 ps after

the pumping pulse. Later, we will compare our time-resolved measurements to these theoretical results.

4.1.4 Previous Evidence for Superfluorescence from Quantum Wells

Previously, at the Magnet Lab in Tallahassee, Jho et al. have measured the time-integrated photoluminescence in high magnetic fields under a variety of circumstances for an $In_{0.2}Ga_{0.8}As$ quantum well sample with the same structure as the sample studied in this work in order to provide evidence for SF [8, 9]. The magnetic field dependent high-intensity PL data was taken using a 31 Tesla Bitter-type magnet and a 150 fs amplified Ti:Sapphire laser. Their edge-collected PL data is similar to the data presented in Section 3.3. Figure 4.7 shows the intensity and linewidth of the 00LL as a function of magnetic field and pump fluence for different excitation spot sizes. When the spot size was 0.5 mm, at a fixed pump fluence, the emission strength scaled as $B^{1.48}$ and the linewidth increased for magnetic fields above 14 Tesla. At fields below 14 Tesla the emission strength scaled linearly with B and the linewidth decreases. These facts indicate that with increasing density, as the magnetic field increases, the dominant type of emission transitions from spontaneous emission with broad linewidth to ASE with a decreasing linewidth due to gain narrowing, both of which scale linearly in strength with increasing field, followed by SF emission that results in a broadening of linewidth and the expected scaling of emission strength (Equation 4.5). The fluence dependent data, at fixed magnetic fields, confirmed this type of analysis by showing a linear dependence at low fluence, decreasing linewidth as the gain increases (ASE), and a superlinear, $N^{1.46}$, intensity scaling in intermediate fluences with broadening of linewidth (SF). The return to linear scaling of emission strength at highest fluences and saturation of linewidth indicate that the 00LL be-

comes full and higher LLs begin to be populated. The other two spot sizes showed mostly a linear scaling with increasing fluence. The linewidth dropped quickly with the larger spot size and took longer to decrease with smaller spot size. This indicates that SF never dominates in either case, only in the 0.5 mm spot size, corresponding to the predicted coherence length for SF emission, at high field and high pump fluence. All of the spectra used for this analysis were integrated over 1000 excitation pulses.

Next, a study of the directionality of the emission after single pulse excitation showed even more convincing evidence for SF. Figure 4.8 shows the experimental geometry and result for single pulse excitation. Two edge fibers were mounted next to two different sides of the sample with μ-prisms to redirect the in-plane emission and simultaneously measure the spectra using the same CCD spectrometer. A pulse picker was used to reduce the repetition rate to 20 Hz in order to ensure emission was collected after single pulse excitation. Data was taken for low and high pump fluences, which correspond to the ASE dominated and SF dominated regime, respectively. Spectra are plotted for selected shots to show that SF emission can alternate in its direction between edge 1 and edge 2 under identical pumping conditions. The normalized emission strength vs. shot number show more clearly an anticorrelation between directions of emission in the high fluence regime and omnidirectional emission in the low fluence regime. An SF pulse consumes almost all of the electron-holes along its path, leaving a narrow, unpumped stripe a few μm in width. This suppresses an additional SF pulse from crossing this path and leads to an anticorrelation between emission directions. This data is the most convincing previous evidence for SF in semiconductor quantum wells.

Finally, the excitation shape was modified by using a cylindrical lens to create a rodlike 3 mm by 0.5 mm excitation region in order to control the SF emission

orientation. Figure 4.9 shows the experimental geometry and spectra after using the cylindrical lens. The angle, θ, is measured between the long beam axis and the direction from excitation to edge 2 fiber. The spectra for edge 1 and edge 2 at $\theta = 0°$ and $\theta = 90°$ shows that the difference in emission strength for the two directions is a factor of $\sim$20. Plotting the emission strength for the 00LL as a function of θ shows that the emission is highly directional with a full width at half maximum of 40° which is comparable to the computed acceptance angle using μ-prisms to redirect the in-plane emission. This directional emission can be expected for both ASE and SF so it is not sufficient evidence by itself to claim SF emission.

4.2 Direct Experimental Observation of Superfluorescence in Quantum Wells

We have performed time-resolved absorption and time-resolved PL measurements using the same $In_{0.2}Ga_{0.8}As$ quantum well sample that was described in Section 3.2.1. Our results provide, for the first time, direct time-domain evidence for SF in a quantum well sample placed in a strong magnetic field.

4.2.1 Methods

The sample preparation method and equipment used are the same as the ones described in Section 4.2. In order to provide time-resolution, we used the OPA and the amplified Ti:Sapphire for a two-color delay stage transmission pump-probe experiment, and we used a 2 ps resolution streak camera to measure the time-resolved PL.

Pump-Probe

Figure 4.10 shows a schematic diagram illustrating the basic experimental procedure. Upon optical excitation, using the amplified Ti:Sapphire laser with photon energy centered at 1.55 eV and pulse width of ~150 fs, electrons are excited well above the GaAs barriers leaving holes in the valence band. Both the electrons and holes experience many scattering events before relaxing to the bottom of the quantum well to form initially incoherent 2D magneto-excitons. In order to study the population dynamics of the magneto-exciton state as a function of LL index, we tuned the OPA to the energy separation between the conduction and valence band LLs. We used the OPA to probe the population inversion of the 00, 11, and 22 transitions as a function of time using standard delay stage pump-probe techniques. Depending on the magnetic field, LL index, and temperature, the probe energies of the transitions varied from 1.30 to 1.41 eV. On an optical table the pump and probe were made collinear before entering the bottom of the magnet bore through the CaF_2 window. The low intensity probe was collected with the center collection fiber and then, outside of the magnet, filtered using a small monochromator tuned to a specific transition before being collected with a silicon photodiode and measured with a lock-in amplifier at the modulation frequency of an optical chopper introduced in the path of the pump line. The lock-in signal was averaged over 1000 pump pulses for each time delay between pump and probe. For the 00, 11, and 22 LLs, we made measurements at magnetic fields of 0, 10, 12.5, 15, and 17.5 Tesla with a fixed temperature of ~5 K and fixed pump power of 5 μJ, and we made measurements at temperatures of 5, 50, 100, and 150 K with a fixed magnetic field of 17.5 Tesla and fixed pump power of 5 μJ.

Time-Resolved Photoluminescence

We also measured the time-resolved PL using a streak camera with 2 ps resolution. The output from either the center- or edge-collection fiber was collimated, filtered, and focused into the streak camera. A set of optical bandpass filters with 10 nanometer width were used to isolate the emission from the individual transitions before entering the streak camera. In order to calibrate the timing of the time-resolved PL, we sent the OPA, tuned to the wavelength of the PL emission, through the appropriate fiber and measured the OPA with the streak camera under the condition that the OPA and amplified Ti:Sapphire laser are incident on the sample at the same time and there is no change in optics between the OPA measurement and the time-resolved PL measurement. By measuring the OPA with the streak camera, we were able to determine our time-resolution of this setup to be $\sim$23 ps. The main limitation for our time-resolution is the multi-mode optical fiber used to collect the PL. Unfortunately, there is no alternative and multi-mode fiber is the best option. Initially, we did not use a grating in conjunction with the streak camera so the horizontal axis of the streak images provided no additional information. The emission collected directly behind the excitation spot predominantly includes only typical spontaneously emitted PL which is emitted in all directions with equal probability. The emission collected in the center collection fiber should be roughly proportional to the population inversion of the transition. ASE as well as SF will travel predominantly in the plane of the quantum wells. Therefore, the edge collected emission should include spontaneously emitted PL, ASE, as well as SF. We made an attempt to use a spectrometer to spectrally resolve the PL before entering the streak camera making the horizontal axis of the streak images correspond to wavelength. Further work is needed to complete setting up the spectrometer for use in conjunction with the streak camera. All measurements

were taken by averaging over 10,000 pump pulses.

4.3 Experimental Results

Pump-Probe

Figure 4.11 shows the magnetic field and temperature dependent results of the pump-probe measurements. The graphs (**a**) and (**b**) show the differential transmission as a function of time for the 11LL and 22LL at different magnetic fields. As the magnetic field increases, a sharp reduction in population develops at earlier delay times for both the 11LL and 22LL. Notice that the 22LL depopulates (at ~50 ps) just a little before the 11LL (at ~70 ps), meaning that the electron-hole pairs in the 22LL did not simply relax down to the full 11LL but instead the carriers left the system in some other way. The graph (**c**) shows the temperature dependence on the differential transmission for the 22LL at 17.5 Tesla. With increasing temperature, the sharp reduction in population happens at later time delay until it no longer occurs at 150 K. The 00LL results are not shown because they show no obvious features with increasing magnetic field. One experimental problem encountered was the existence of pre- and post-pulses ~900 ps away from the main pulse coming out of the amplified Ti:Sapphire laser. Even though these pulses were measured in a long cross correlation to be ~100 times weaker than the main pulse, the 00LL showed a finite differential transmission signal before the time zero delay between the main pump pulse and the probe pulse. The 00LL is the lowest energy transition so it should be expected that it would be the most sensitive to a pre-pulse.

Time-Resolved Photoluminescence

Figure 4.12 shows the edge-collected streak camera results as a function of magnetic field for the first three LLs at 5 K and 5 μJ pump energy. With increasing magnetic field, we can see oscillations in the time-resolved PL for the 00LL. They increase in intensity and occur at shorter time delays. For the higher LLs, we see no dramatic pulse at 10 T but we do see a large pulse at higher magnetic fields at a time delay of ~150-200 ps. This figure has been corrected for the intensity for each graph individually. At 17.5 Tesla, the 11LL has lower intensity than the other magnetic fields. At this magnetic field, the separation between the 00 and 11 LLs is very close to the longitudinal optical phonon energy, ~36.5 meV, for GaAs which should be close to the value for the $In_{0.2}Ga_{0.8}As$ quantum well, and we suspect that there is relaxation into the 00LL due to this fact.

Figure 4.13 shows the power dependent data for the first three LLs at 5 K and 15 Tesla. As the power is increased, it appears that a pulse forms at ~200 ps and at the highest power a large pulse forms at ~100 ps for the higher LLs.

Figure 4.14 shows the temperature dependent data for the 11 and 22 LLs at 15 Tesla and 5 μJ pump energy. It is clear that pulse-like features move to greater time delay with increasing temperature. Even at 150 K, a pulse feature is observed for the 22LL.

Figure 4.15 shows our initial results using a spectrometer to spectrally resolve the PL before entering the streak camera. This figure is obtained by putting three streak images next to each other. We were not able to calibrate the timing or wavelength correctly for these results. However, they are promising in the sense that we see clear pulses of radiation from all three LLs.

4.4 Discussion and Future Work

Our pump-probe measurements (Figure 4.11) show a sudden drop in population after a delay time of ~50 ps for the 22LL at highest magnetic field and lowest temperature, which is in very good agreement with the theoretical result (Figure 4.6). Also, the differential transmission as a function of time changes in the expected manner when increasing temperature or increasing magnetic field. With increasing temperature, the sudden drop in population moves to later time delay and eventually disappears because T_2 decreases with increasing temperature making it more difficult to build the macroscopic polarization necessary for a SF pulse. Increasing the magnetic field increases the density of states and, in turn, increases the growth rate of macroscopic polarization which we observe as the sudden drop in population occurring at shorter time delays with increasing magnetic field. Overall, the pump-probe measurements provide the most convincing evidence that the electron-hole populations disappear by way of a SF pulse.

The time-resolved PL measurements show large pulse features under the conditions of high magnetic field, high pump energy, and low temperature. Overall, these pulses of radiation occur under the expected conditions. However, for some of the data collected, such as the 11 and 22 LL at 17.5 Tesla, the intensity is much weaker than expected in comparison to the 12.5 and 15 Tesla cases. Furthermore, there are often many pulse-like features that make it difficult to distinguish which ones are the SF pulse and which are ASE features. There are also problems associated with the calibration of the timing. Because there is some slow overall drift in the triggering of the streak camera, there may be a slight change, ~10-20 ps, in timing between the PL measurement and the OPA calibration measurement.

In order to fully understand all of the emission dynamics, it will be necessary

to provide spectral resolution and time resolution simultaneously. Our initial results show promise, but we did not have the correct grating to measure all three LLs and a timing reference pulse at the same time. This will be the primary goal of future measurements. By using a spectrometer in conjunction with the streak camera, we will avoid the problems associated with using optical filters to isolate the emission from particular LLs. Although each filter was selected for a given transition, under some circumstances the peak spectral position did not exactly correspond to the center wavelength of the bandpass filter. Furthermore, by measuring a reference pulse from the OPA tuned to a wavelength with photon energy less than the lowest energy emission and incident on the sample at the same time as the excitation source, we will have a reference time zero during the measurement. This should reduce the errors in timing due to an overall drift on the triggering of the streak camera.

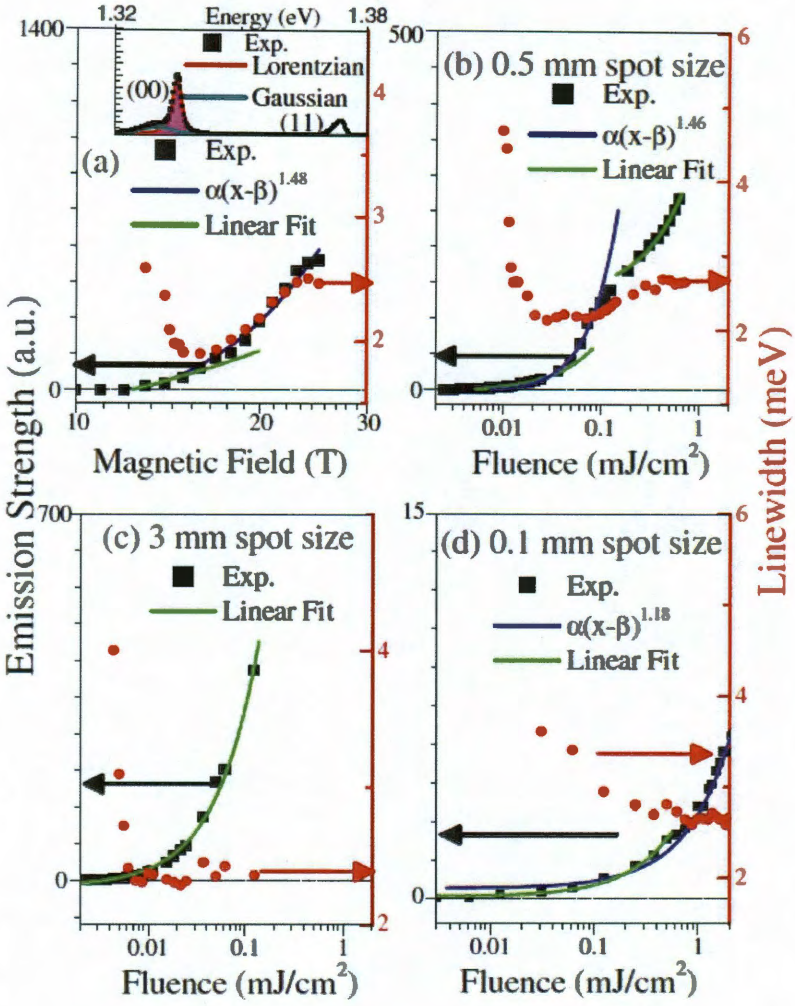

Figure 4.7 : 00LL emission strength and linewidth as a function of magnetic field and pump fluence for spot sizes: 0.5 mm (**a**) (**b**), 3 mm (**c**), and 0.1 mm (**d**). A superlinear dependence on magnetic field (**a**) and pump fluence (**b**) was observed indicating SF emission. No such dependence was observed with the spot sizes (**c**) (**d**) that do not correspond to the predicted coherence length for SF in this $In_{0.2}Ga_{0.8}As$ quantum well sample [8].

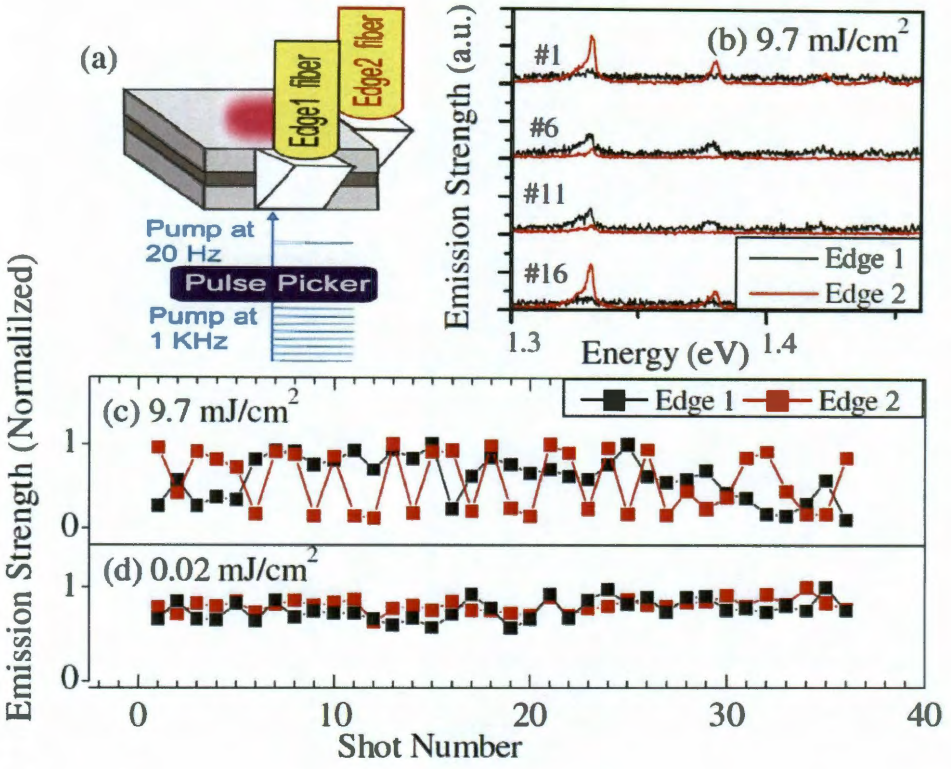

Figure 4.8 : Pulse to pulse fluctuations in emission direction were observed by using two edge fibers (**a**) to simultaneously measure the spectra after single pulse excitation for many experimental shots (**b**). Normalized emission strength vs. shot number were plotted to show an anticorrelation for high pump fluence (**c**) and correlation for low pump fluence [8].

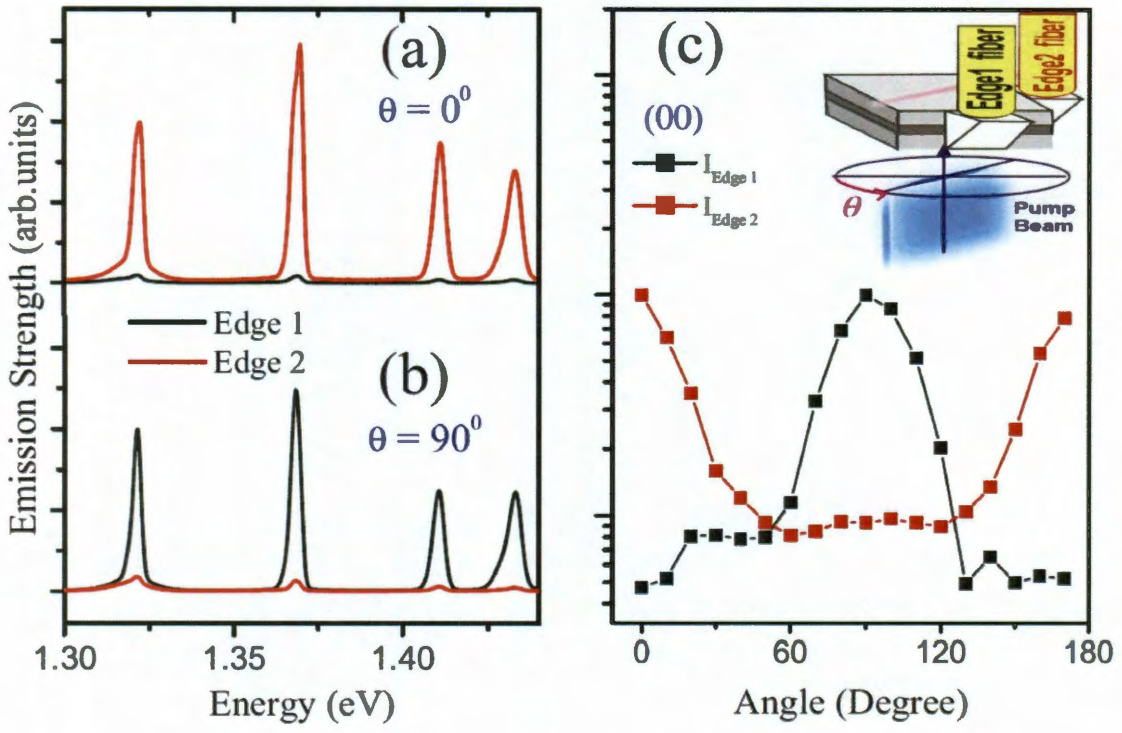

Figure 4.9 : Spectra (**a**) (**b**) obtained from edge 1 and edge 2 while rotating the long axis of a rodlike excitation region. θ was measured as the angle from the axis of the excitation line to edge 2 (**c**). The full width at half maximum of the emission strength of the 00LL was 40° roughly corresponding to the calculated acceptance angle of the μ-prisms showing strong directionality of the emission [9].

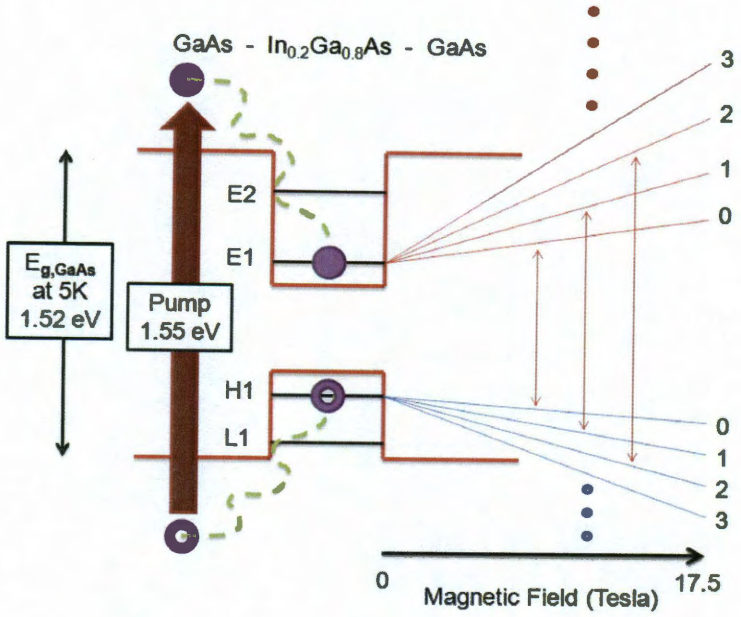

Figure 4.10 : Schematic diagram showing the energy levels investigated via the pump-probe experiment. Electrons were pumped well above the GaAs barriers leaving holes in the valence band where many scattering events occured to leave them initially completely incoherent in the $In_{0.2}Ga_{0.8}As$ quantum wells. We probed the LL populations as a function of time delay between the pump and probe.

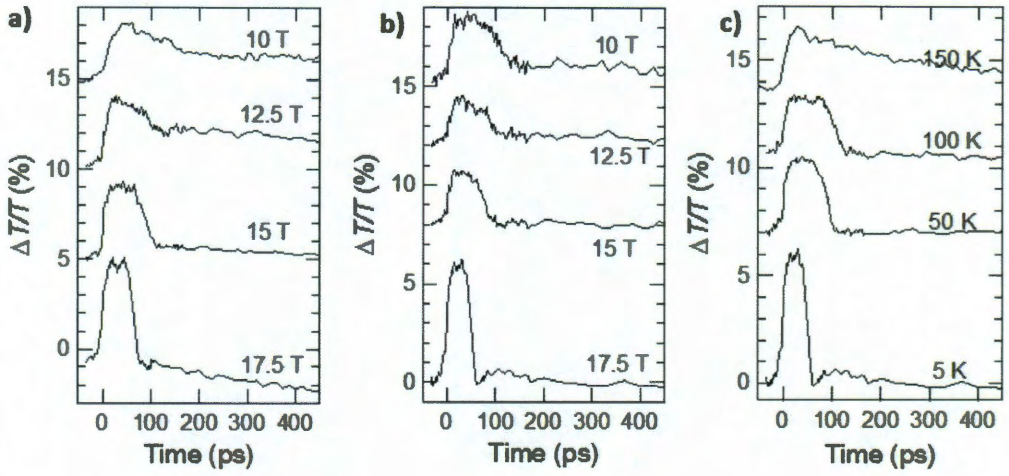

Figure 4.11 : Results from the pump-probe measurements. Magnetic field dependence for the (**a**) 11LL and (**b**) 22LL at 5 K and 5 μJ pump energy. Temperature dependence results for the 22LL at 17.5 Tesla and 5 μJ pump energy (**c**). There was a sudden drop in population after some time delay at high magnetic fields and low temperatures. Adapted from [7].

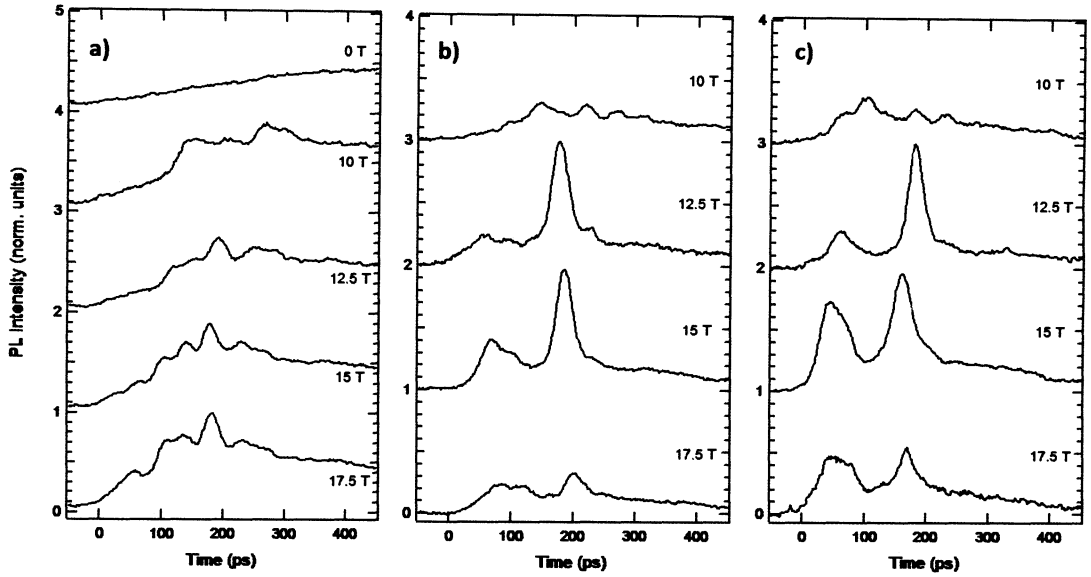

Figure 4.12 : Magnetic field dependence on the time-resolved photoluminescence measurement for the (**a**) 00LL, (**b**) 11LL, and (**c**) 22LL at 5 K and 5 μJ pump energy. Large pulse features indicative of SF emission emerged at high magnetic fields.

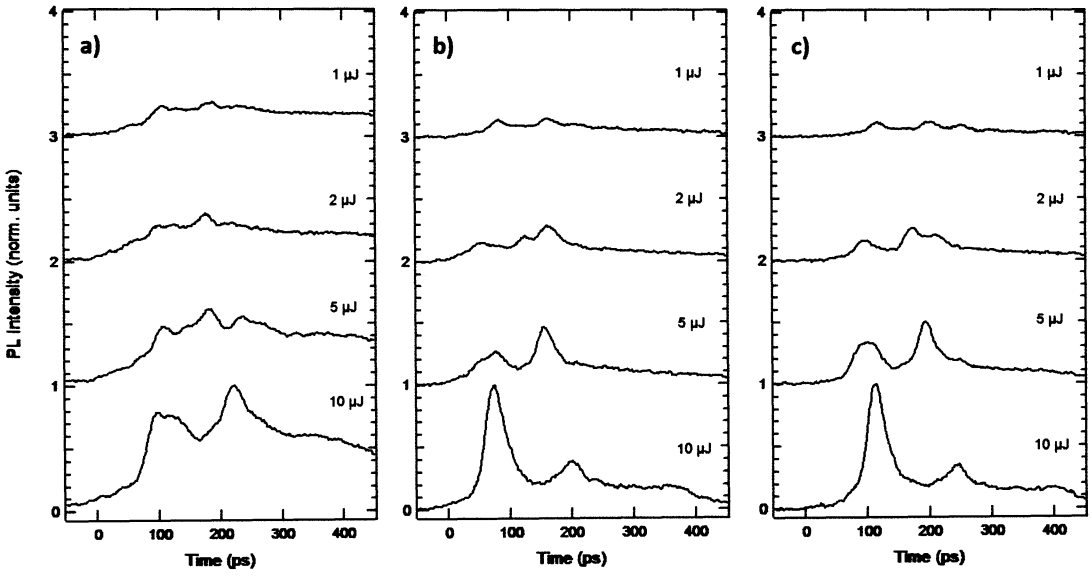

Figure 4.13 : Power dependence on the time-resolved photoluminescence measurement for the (**a**) 00LL, (**b**) 11LL, and (**c**) 22LL at 5 K and 15 Tesla. Large pulse features indicative of SF emission emerged at high pumping powers.

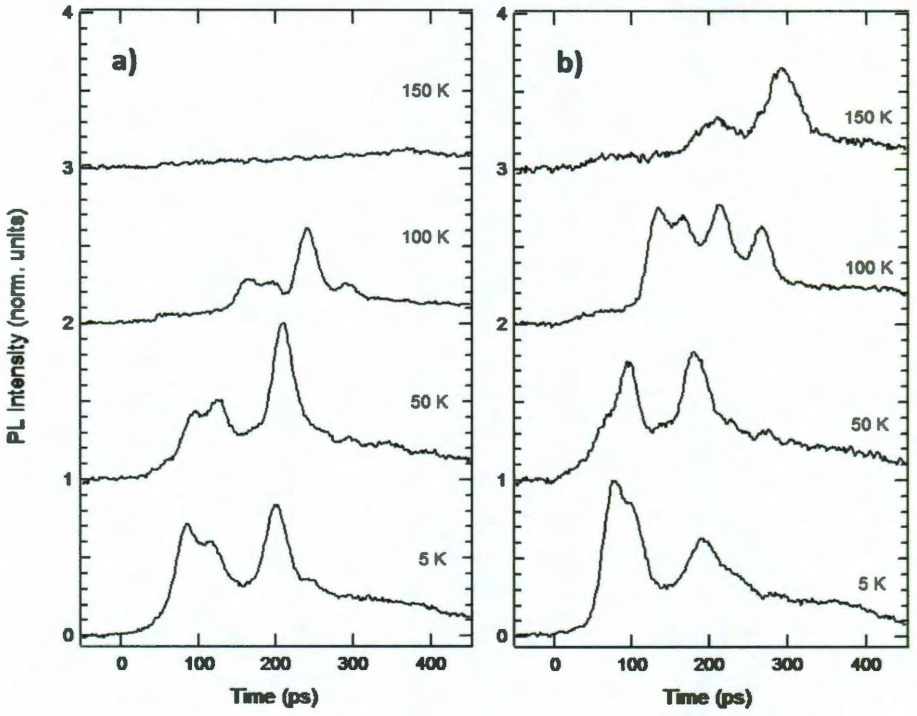

Figure 4.14 : Temperature dependence on the time-resolved photoluminescence measurement for the (**a**) 11LL and (**b**) 22LL at 15 Tesla and 5 μJ pump energy. The SF pulses move to later time delay after the pump with increasing temperature.

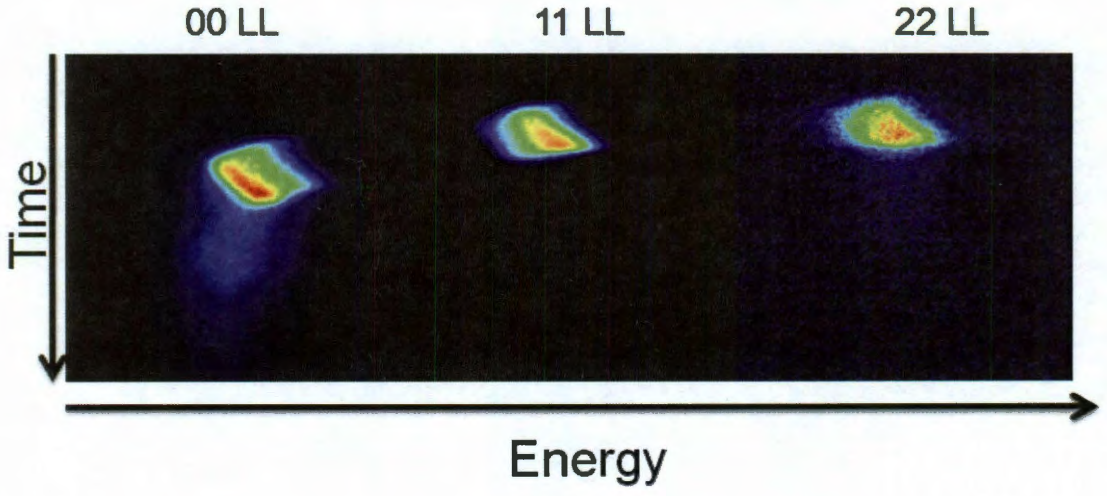

Figure 4.15 : Spectrally resolved streak camera images for all three LLs at 5K, 15 Tesla, and 10 μJ pump energy. SF emission is observed for all three LLs.

Chapter 5

Conclusions

In conclusion, we have used ultrafast spectroscopy techniques to measure two different types of semiconductor heterostructures. For the InAs/GaSb based short-period superlattice samples, we measured the carrier and phonon dynamics in time ranges from $\sim$100 fs to $\sim$5 μs. Our results can provide information about the long carrier lifetime as well as interface quality in order to optimize the growth conditions for the purpose of creating a material to use for mid-IR detection that can operate at high temperatures.

We also measured the time-integrated PL and time-resolved PL and absorption using an $In_{0.2}Ga_{0.8}As$ quantum well sample placed in high magnetic fields. Our time-integrated PL measurements indicate that single-exciton emission can be observed from a dense electron-hole magnetoplasma under the conditions of gain and magnetic field. These results extend the concept of the "hidden symmetry" predicted to exactly cancel all interexciton interactions in an electron-hole magnetoplasma. Our time-resolved measurements show a sharp reduction in electron-hole population after some time delay and large pulsed radiation emitted in the plane of the quantum wells. These results provide the first direct time-domain evidence for SF in a semiconductor quantum well sample in high magnetic fields.

Bibliography

[1] N. Miura, *Physics of Semiconductors in High Magnetic Fields.* Oxford University Press, 2008.

[2] R. Dingle, "Confined Carrier Quantum States in Ultrathin Semiconductor Heterostructures," *Festkörperprobleme (Advances in Solid State Physics)*, vol. XV, pp. 21–47, 1975.

[3] J. Lee, G. Noe, Y. Wang, C. Stanton, G. Solomon, A. Belyanin, D. Reitze, and J. Kono, "Robust, Stable Single-Exciton Emission from an Ultrahigh-Density Magneto-Plasma," arXiv:1009.3067v1[cond-mat.mes-hall].

[4] N. Skribanowitz, I. Herman, J. MacGillivray, and M. Feld, "Observation of Dicke Superradiance in Optically Pumped HF Gas," *Phys. Rev. Lett.*, vol. 30, no. 8, pp. 309–312, 1973.

[5] M. Gross, C. Fabre, P. Pillet, and S. Haroche, "Observation of Near-Infrared Dicke Superradiance on Cascading Transitions in Atomic Sodium," *Phys. Rev. Lett.*, vol. 36, no. 7, pp. 1035–1038, 1976.

[6] H. Gibbs, Q. Vrehen, and H. Hikspoors, "Single-Pulse Superfluorescence in Cesium," *Phys. Rev. Lett.*, vol. 39, no. 9, pp. 547–550, 1977.

[7] G. Noe, J. Lee, Y. Wang, A. Wojcik, S. McGill, G. Solomon, A. Belyanin, D. Reitze, and J. Kono, "Delayed bursts of coherent light from quantum wells: direct

evidence of excitonic superfluorescence," *Nature*, in preparation.

[8] Y. Jho, X. Wang, J. Kono, D. Reitze, X. Wei, A. Belyanin, V. Kocharovsky, V. Kocharovsky, and G. Solomon, "Cooperative Recombination of a Quantized High-Density Electron-Hole Plasma in Semiconductor Quantum Wells," *Phys. Rev. Lett.*, vol. 96, no. 237401, pp. 1–4, 2006.

[9] Y. Jho, X. Wang, D. Reitze, J. Kono, A. Belyanin, V. Kocharovsky, V. Kocharovsky, and G. Solomon, "Cooperative recombination of electron-hole pairs in semiconductor quantum wells under quantizing magnetic fields," *Phys. Rev. B*, vol. 81, no. 155314, pp. 1–12, 2010.

[10] R. Hall, G. Fenner, J. Kingsley, T. Soltys, and R. Carlson, "Coherent Light Emmission From GaAs Junctions," *Phys. Rev. Lett.*, vol. 9, no. 9, pp. 366–368, 1962.

[11] M. Nathan, W. Dumke, G. Burns, F. Dill Jr., and G. Lasher, "Stimulated Emission of Radiation From GaAs p-n Junctions," *Appl. Phys. Lett.*, vol. 1, no. 3, pp. 62–64, 1962.

[12] H. Kroemer, "A Proposed Class of Heterojunction Injection Lasers," *Proc. IEEE*, vol. 51, pp. 1782–1783, 1963.

[13] A. Cho and J. Arthur, "Molecular Beam Epitaxy," *Prog. Solid State Chem.*, vol. 10, pp. 157–191, 1975.

[14] J. Singh, *Physics of Semiconductors and Their Heterostructures.* McGraw-Hill, Inc., 1993.

[15] C. Weisbuch and B. Vinter, *Quantum Semiconductor Heterostructures.* Academic Press, 1991.

[16] P. Smith, D. Auston, and M. Nuss, "Subpicosecond photoconducting dipole antennas," *IEEE J. Quantum Electon.*, vol. 24, pp. 255–260, 1988.

[17] J. Shah, *Ultrafast Spectroscopy of Semiconductors and Semiconductor Nanostructures.* Springer, 1996.

[18] R. Dicke, "Coherence in Spontaneous Radiation Processes," *Phys. Rev.*, vol. 93, pp. 99–110, 1954.

[19] E. Youngdale, J. Meyer, C. Hoffman, F. Bartoli, C. Grein, P. Young, H. Ehrenreich, R. Miles, and D. Chow, "Auger lifetime enhancement in InAs-$Ga_{1-x}In_xSb$ superlattices," *Appl. Phys. Lett.*, vol. 64, pp. 3160–3162, 1994.

[20] C. Grein, P. Young, and H. Ehrenreich, "Minority carrier lifetimes in ideal InGaSb/InAs superlattices," *Appl. Phys. Lett.*, vol. 61, pp. 2905–2907, 1992.

[21] D. Donetsky, S. Svensson, L. Vorobjec, and G. Belenky, "Carrier lifetime measurements in short-period InAs/GaSb strained-layer superlattice structures," *Appl. Phys. Lett.*, vol. 95, no. 212104, 2009.

[22] G. Sanders, C. Stanton, J. Wang, J. Kono, A. Oiwa, and H. Munekata, "Theory of carrier dynamics and time resolved reflectivity in $In_xMn_{1-x}As$/GaSb heterostructures," *Phys. Rev. B*, vol. 72, no. 245302, 2005.

[23] C. Sun, J. Liang, C. Stanton, A. Abare, L. Coldren, and S. DenBaars, "Large coherent acoustic-phonon oscillation observed in InGaN/GaN multiple-quantum wells," *Appl. Phys. Lett.*, vol. 75, pp. 1249–1251, 1999.

[24] G. Sanders, C. Stanton, and C. Kim, "Theory of coherent acoustic phonons in $In_xGa_{1-x}N/GaN$ multiple quantum wells," *Phys. Rev. B*, vol. 64, no. 235316, 2001.

[25] T. Dekorsy, R. Taubert, F. Hudert, G. Schrenk, A. Bartels, R. Cerna, V. Kotaidis, A. Plech, K. Köhler, J. Schmitz, and J. Wagner, "High-speed asynchronous optical sampling for high-sensitivity detection of coherent phonons," *J. Phys.: Conf. Ser.*, vol. 92, no. 012005, 2007.

[26] M. Balkanski and R. F. Wallis, *Semiconductor Physics and Applications*, pp. 409–410. Oxford University Press, 2000.

[27] O. Akimoto and H. Hasegawa, "Interband Optical Transitions in Extremely Anisotropic Semiconductors. II. Coexistence of Excitons and the Landau Levels," *J. Phys. Soc. Japan*, vol. 22, pp. 181–191, 1967.

[28] A. MacDonald and D. Ritchie, "Hydrogenic energy levels in two dimensions at arbitrary magnetic fields," *Phys. Rev. B*, vol. 33, pp. 8336–8344, 1986.

[29] N. Mott, "The transition to the metallic state," *Phil. Mag.*, vol. 6, pp. 287–309, 1961.

[30] A. Dzyubenko and Y. Lozovik, "Symmetry of Hamiltonians of quantum two-component systems: condensate of composite particles as an exact eigenstate," *J. Phys. A*, vol. 24, pp. 415–424, 1991.

[31] G. Finkelstein, H. Shtrikman, and I. Bar-Joseph, "Mechanism of shakeup processes in the photoluminescence of a two-dimensional electron gas at high magnetic fields," *Phys. Rev. B*, vol. 56, no. 10326, 1997.

[32] E. Rashba, M. Sturge, H. Yoon, and L. Pfeiffer, "Hidden symmetry and the magnetically induced "Mott transition" in quantum wells containing an electron gas," *Solid State Commun.*, vol. 114, pp. 593–596, 2000.

[33] Y. Jho, F. Kyrychenko, J. Kono, X. Wei, S. Crooker, G. Sanders, D. Reitze, C. Stanton, and G. Solomon, "Role of Coulomb interactions in dark-bright magnetoexciton mixing in strained quantum wells," *Phys. Rev. B*, vol. 72, no. 045340, 2005.

[34] L. Butov, V. Egorov, and V. Kulakovskii, "Magnetoluminescence study of many-body effects in a dense electron-hole plasma of strained $In_xGa_{1-x}As$ quantum wells," *Phys. Rev. B*, vol. 46, pp. 15156–15162, 1992.

[35] A. E. Siegman, *Lasers.* University Science Books, 1986.

[36] R. Bonifacio and L. Lugiato, "Cooperative radiation processes in two-level systems: Superfluorescence," *Phys. Rev. A*, vol. 11, no. 5, pp. 1507–1521, 1975.

[37] R. Glauber and F. Haake, "The Initiation of Superfluorescence," *Phys. Lett.*, vol. 68A, no. 1, pp. 29–32, 1978.

[38] D. Polder, M. Schuurmans, and Q. Vrehen, "Superfluorescence: Quantum-mechanical derivation of Maxwell-Bloch description with fluctuating field source," *Phys. Rev. A*, vol. 19, no. 3, pp. 1192–1203, 1979.

[39] A. Belyanin, V. Kocharovsky, and V. Kocharovsky, "Collective QED processes of electron-hole recombination and electron-positron annihilation in a strong magnetic field," *Quantum Semiclass. Opt.*, vol. 9, pp. 1–44, 1997.